

NASA TECHNICAL NOTE



NASA TN D-4654

c. 1

NASA TN D-4654

LOAN COPY: RETURN
TO: (SVCIL-2)
CINCINNATI AFB, OHIO



RADIOMETRIC MEASUREMENTS OF THE
EARTH'S INFRARED HORIZON FROM THE X-15
IN THREE SPECTRAL INTERVALS

*by Antony Jalink, Jr., Richard E. Davis,
and Dwayne E. Hinton*

*Langley Research Center
Langley Station, Hampton, Va.*



TECH LIBRARY KAFB, NM



0131380

RADIOMETRIC MEASUREMENTS OF THE EARTH'S INFRARED HORIZON
FROM THE X-15 IN THREE SPECTRAL INTERVALS

By Antony Jalink, Jr., Richard E. Davis,
and Dwayne E. Hinton

Langley Research Center
Langley Station, Hampton, Va.

NATIONAL AERONAUTICS AND SPACE ADMINISTRATION

For sale by the Clearinghouse for Federal Scientific and Technical Information
Springfield, Virginia 22151 - CFSTI price \$3.00

RADIOMETRIC MEASUREMENTS OF THE EARTH'S INFRARED HORIZON
FROM THE X-15 IN THREE SPECTRAL INTERVALS

By Antony Jalink, Jr., Richard E. Davis,
and Dwayne E. Hinton
Langley Research Center

SUMMARY

Experimental data of the earth's horizon in three spectral intervals, 0.8 to 2.8 μm , 10 to 14 μm , and 14 to 20 μm , have been obtained by using the X-15 research airplane. The resolution (field of view) of the data at the tangent point is approximately 2 kilometers, and the spatial position of the horizon profile is known to within 4 kilometers.

The 14 to 20 μm interval was shown to be the best spectral interval for horizon sensing because it exhibits the least variance at adequate radiant intensity. The 0.8 to 2.8 μm and 10 to 14 μm spectral intervals do not appear suitable for accurate horizon sensing because they are sensitive to low-altitude meteorological changes.

The experimental data obtained verified, within experimental accuracy, the theory used to predict the far infrared radiant energy due to carbon dioxide. The use of theory for spectral regions where high-altitude water-vapor data are required is questionable because no mixing-ratio information is available. The single-scattering theory cannot predict accurately the radiant energy in the near infrared region ($<3.0 \mu\text{m}$).

INTRODUCTION

Conventional flight-vehicle attitude instruments use gravity sensors to determine the local vertical. In orbital vehicles, which are in essentially a "zero g" condition, such instruments become useless. As an alternative, when the space vehicle is in the vicinity of the earth, the apparent horizon formed either by thermal emission or by scattered and reflected sunlight from the earth and its atmosphere can be sensed against the effective temperature of interstellar space (3.1°K) to determine vehicle attitude. Ideally, the radiation profile sensed by a horizon scanner when it scans from space onto the earth should be well defined; that is, it should be steep and invariant. However, the radiation gradient is affected by meteorological conditions, solar irradiance, location on earth, and the spectral interval employed by the sensor. Knowledge of the effect of these factors on the infrared characteristics of the earth's radiance profile determines, to a great extent, the positional accuracy and reliability attainable by horizon-sensing methods.

In order to obtain experimental measurements of the radiation gradient, a program using the X-15 research airplane as a test vehicle (ref. 1) was instituted by the Langley Research Center. A radiometer carried in the tail-cone box of the X-15 was used to view the horizon during the peak-altitude portion of the X-15 flight.

This report presents the horizon-radiance measurements obtained from three flights. The spectral band and data of each flight is as follows:

Flight number	Spectral band	Date
Flight 1	0.8 to 2.8 μm	July 8, 1964
Flight 2	10 to 14 μm	May 28, 1965
Flight 3	14 to 20 μm	June 29, 1965

Meteorological measurements were obtained for each flight to allow construction of calculated radiance profiles based on existing radiance theory for comparison with the measured profiles. This report contains a description of the flight instrumentation employed for the X-15 missions, which includes the design and calibration of the radiometer, the description of the X-15 instrumentation used to obtain the measurements, and the method used to calculate the radiance profile relative to the earth's surface. A discussion of the instrumentation errors and the expected accuracy of the measurement system is given.

SYMBOLS

- A area, centimeters² (cm²)
- B equivalent noise bandwidth, hertz (Hz)
- D diameter of objective, centimeters (cm)
- D* detectivity, centimeter-hertz^{1/2}/watt (cm-Hz^{1/2}/W)
- e water-vapor pressure, millibars (mbar) (1 millibar = 1 hectonewton/meter²)
- F_c focal length of collimator, centimeters (cm)
- F_o focal length of radiometer optics, centimeters (cm)
- f frequency, hertz (Hz)

f_c	corner frequency, hertz (Hz)
$G(j\omega)$	transfer function
g	acceleration due to gravity, meters/second ² (m/sec ²)
H	irradiance, watts/meter ² (W/m ²)
h	tangent height (see fig. 1), kilometers (km)
h_{X-15}	altitude of X-15, kilometers (km)
K	midband gain
K_1, K_2	constants
l	distance, centimeters (cm)
M_1, M_2, M_3, M_4	matrices
N	number of samples
n	number of samples
P_λ	spectral radiant power, watts/micrometer (W/ μ m)
p	total atmospheric pressure, millibars (mbar)
R	radiant emittance, watts/meter ² (W/m ²)
R_λ	spectral radiant emittance, watts/meter ² -micrometer (W/m ² - μ m)
$R_{\omega\lambda}$	spectral radiance, watts/meter ² -steradian-micrometer (W/m ² -sr- μ m)
r	radius of earth, kilometers (km)
T	temperature, degrees Kelvin ($^{\circ}$ K)
t	time, seconds (sec)

t_1, t_2	times of evaluation, seconds (sec)
V_i	initial voltage, volts (V)
V_N	noise voltage, volts (V)
V_S	signal voltage, volts (V)
w	water-vapor mixing ratio, grams/kilogram (g/kg)
X_N	difference between average value and value of sample N
x, y, z	local earth axes
x_a, y_a, z_a	aircraft axes
x_R, y_R, z_R	radiometer axes
x_S, y_S, z_S	space-fixed axes
α	scan mirror angle, degrees (deg)
α_m	vertical mounting angle, degrees (deg)
β	nadir angle, degrees (deg)
η	optical efficiency of system
θ	pitch angle, degrees (deg)
θ_c	error in pitch angle due to platform calibration and recording paper shrinkage, degrees (deg)
θ_R	minimum angle of resolution, degrees (deg)
λ	wavelength, micrometers (μm)
σ	standard deviation

σ_h	standard deviation in tangent height, kilometers (km)
$\sigma_{h_{X-15}}$	standard deviation in X-15 altitude, kilometers (km)
σ_α	standard deviation in scan mirror angle, degrees (deg)
σ_{α_m}	standard deviation in vertical mounting angle, degrees (deg)
σ_θ	standard deviation in pitch angle, degrees (deg)
σ_{θ_c}	standard deviation in error in pitch angle, degrees (deg)
σ_ϕ	standard deviation in roll angle, degrees (deg)
τ	time constant, seconds (sec)
ϕ	roll angle, degrees (deg)
ψ	yaw angle, degrees (deg)
ψ_m	horizontal mounting angle, degrees (deg)
ω	solid angle, steradians (sr)
ω_v	field of view, steradians (sr)

EXPERIMENTAL SYSTEM DESCRIPTION

The horizon profile can be represented by a plot of radiance as a function of tangent height, where tangent height is the minimum altitude of the radiometer line of sight. Tangent height can be computed from the position of the observer and the nadir angle to the line of sight of the radiometer, as shown in figure 1 and derived in appendix A. The nadir angle, in turn, is found from the instantaneous attitude of the aircraft and the angle of the mirror scan. If the calculations are performed in all degrees of freedom, the latitude and longitude of the tangent point are also obtained.

A systems diagram of the X-15 horizon definition experiment is shown in figure 2. The dashed-line boxes indicate available data sources routine to X-15 flights. The solid-line boxes show equipment and calculations provided especially for this experiment. The radiometric output is combined with the calibration data obtained for the instrument so

that the observed radiance is known. From the X-15 stable platform, aircraft pitch, roll, and yaw data are obtained. These data are combined with the radiometer scan mirror angle and aircraft position from ground tracking to obtain the direction and position of the instrument line of sight so that the observed radiance data can be fixed relative to a specific point on earth. A set of data points is extracted from the flight records every 5 msec, and the calculations are performed with the aid of an IBM 7094 computer.

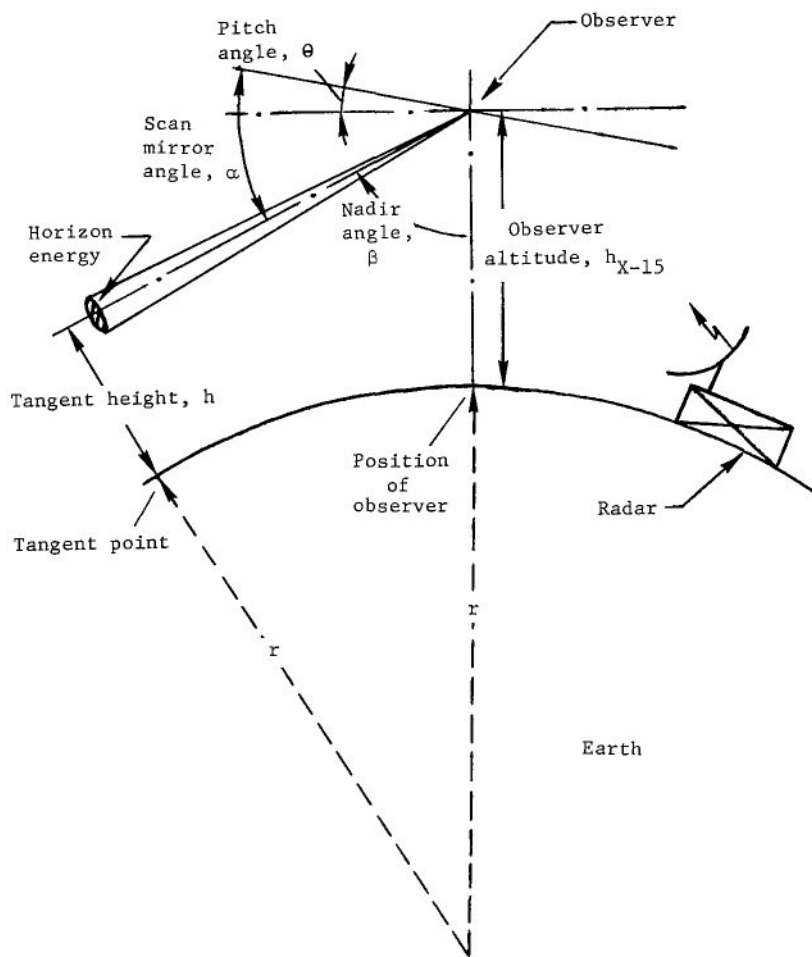


Figure 1.- Geometry of horizon sensing.

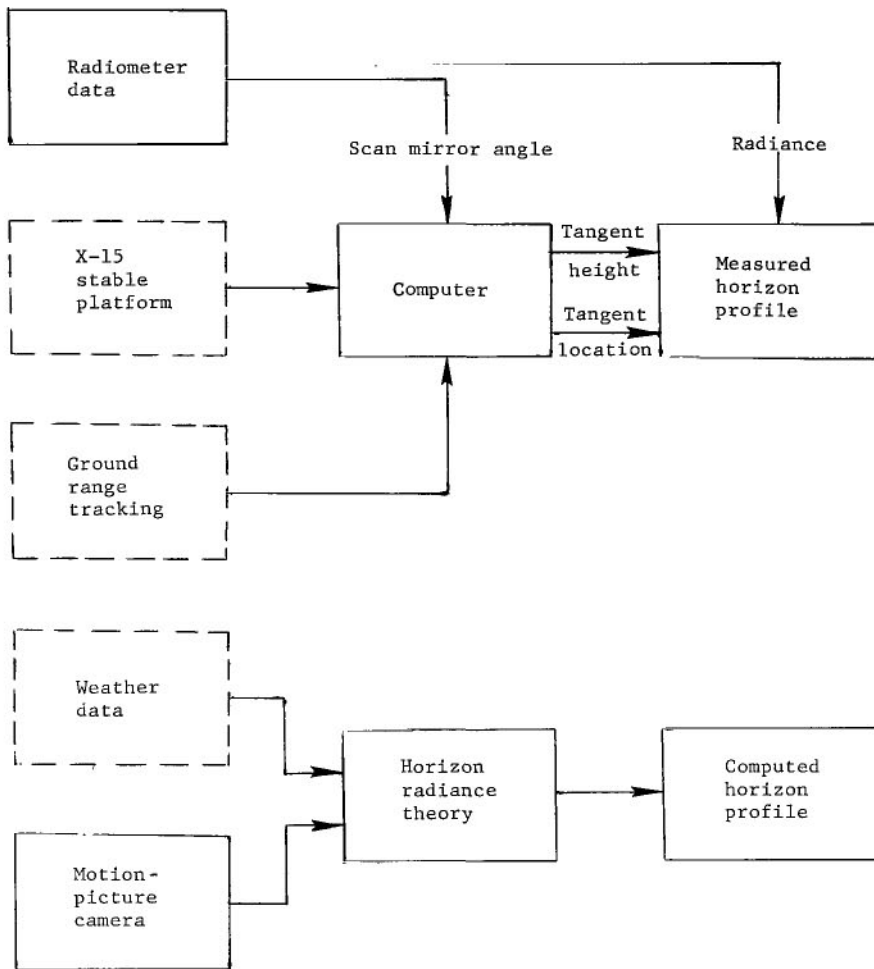


Figure 2.- A systems diagram of X-15 horizon definition experiment.

RADIOMETER DESIGN

The radiometer is mounted in the tail-cone box, immediately behind the vertical stabilizer fin of the X-15 rocket airplane, and looks back out of the rear of the aircraft, as shown in figure 3. Because the tail-cone box is external to the airplane and is not heated, the radiometer is subject to a coldsoak near -50°C prior to launch when the X-15 is carried to an altitude of 14 km by a B-52 aircraft. All structural parts of the radiometer are invar to minimize defocusing of the optics due to the extreme temperature range. Also, the X-15 rocket engine operation results in a 10g vibration environment which the instrument must survive. However, during the data period which occurs at peak altitude the engine is shut down and interference from engine vibration and exhaust is thus eliminated. A 16-mm motion-picture camera mounted beside the radiometer observed the

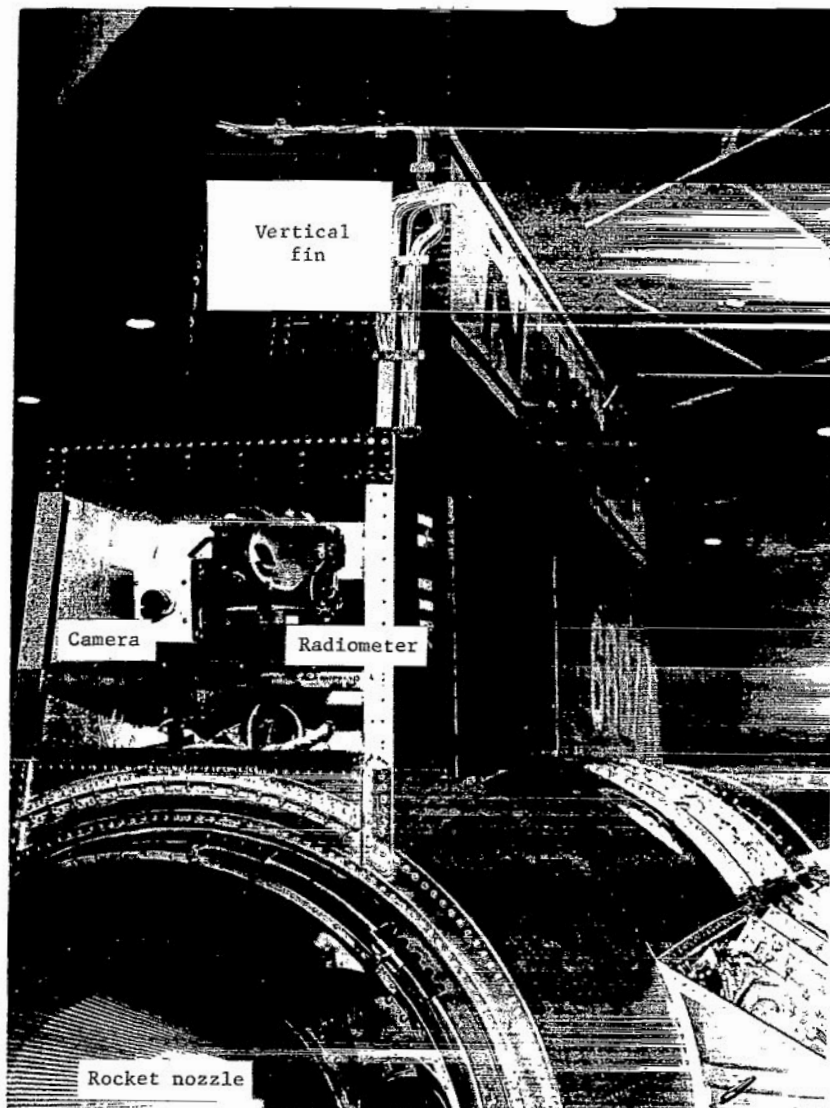


Figure 3.- Radiometer mounted on X-15.

L-68-861

presence of clouds and haze during the data-taking period. Postflight examination and calibration of the radiometer and the film from the camera indicated that combustion products from the rocket exhaust did not measurably contaminate the optics.

A schematic drawing and a photograph of the radiometer are shown in figures 4 and 5, respectively. The radiometer uses a motor-driven scan mirror which sweeps the field of view through a 30° optical scan at a speed of 20° per sec. A precision potentiometer is used to record the mirror position. The scan mirror reflects the energy onto the

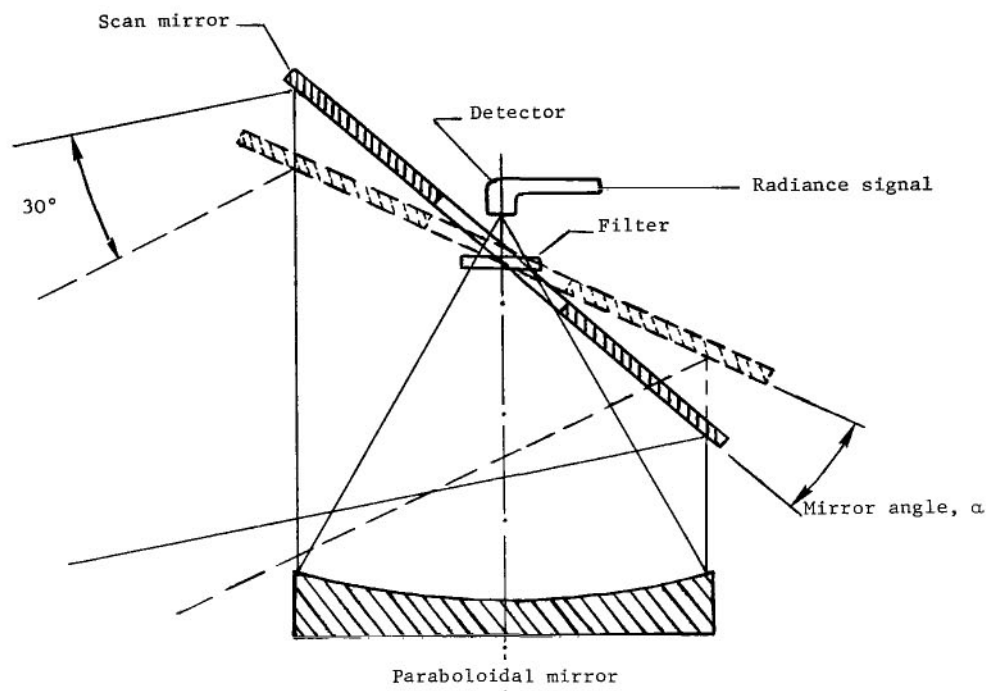


Figure 4.- Schematic drawing of X-15 radiometer. Field of view, 0.13° by 0.13° ; diameter of objective, 12.7 cm.

objective, a 12.7-cm-diameter paraboloidal mirror with an f-number of 1, which focuses the energy onto the detector. The field of view which is determined by the size of the detector, was measured to be 0.13° by 0.13° at the half-response points. This detector size results in a radiometric resolution of 2 km at the horizon tangent point. Because the detectors are affected by changes in the ambient temperature, they are thermostatically controlled within a preset range. The radiation also passes through an optical band-pass filter used to select the spectral region to be investigated. The filter is not heated, because the shift in wavelength due to the expected ambient-temperature range is, at most, 0.8 percent which is thought to be negligible. The optical filter, detector, and electronics are somewhat different for each spectral interval. The radiometer characteristics for each flight are listed in table I and the spectral-response curves are shown in figure 6. A detailed discussion of the characteristics of each detection system and the methods used to calibrate them are given in appendix B.

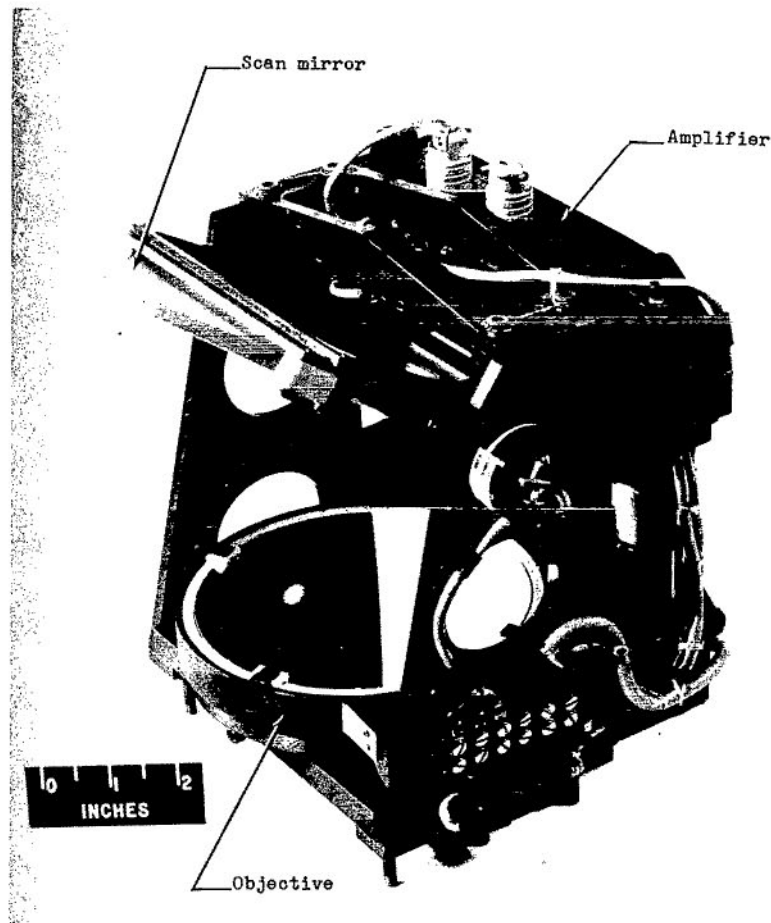


Figure 5.- Photograph of X-15 radiometer.

L-68-862

METEOROLOGICAL INFORMATION FOR THE FLIGHT EXPERIMENT

In order to evaluate the horizon-radiance theory and its ability to predict radiance profiles, it is necessary to obtain information concerning the meteorological conditions existing at the time of each flight. With this information, theoretical radiance profiles may be calculated and compared with the measured radiance profiles.

Many authors (refs. 2, 3, and 4) have formulated procedures to obtain atmospheric radiance profiles in the far infrared region. In the 10 to 14 μm window interval, most of the radiance is received from opaque bodies, such as the earth, and clouds, and is only slightly attenuated by the atmosphere. In the 14 to 20 μm interval, the carbon dioxide (CO_2) and water vapor (H_2O) within the atmosphere provide thermal radiation which is subsequently attenuated by the atmosphere between the radiating element and the detector. In order to calculate the radiance received, it is necessary to know the amount of absorber

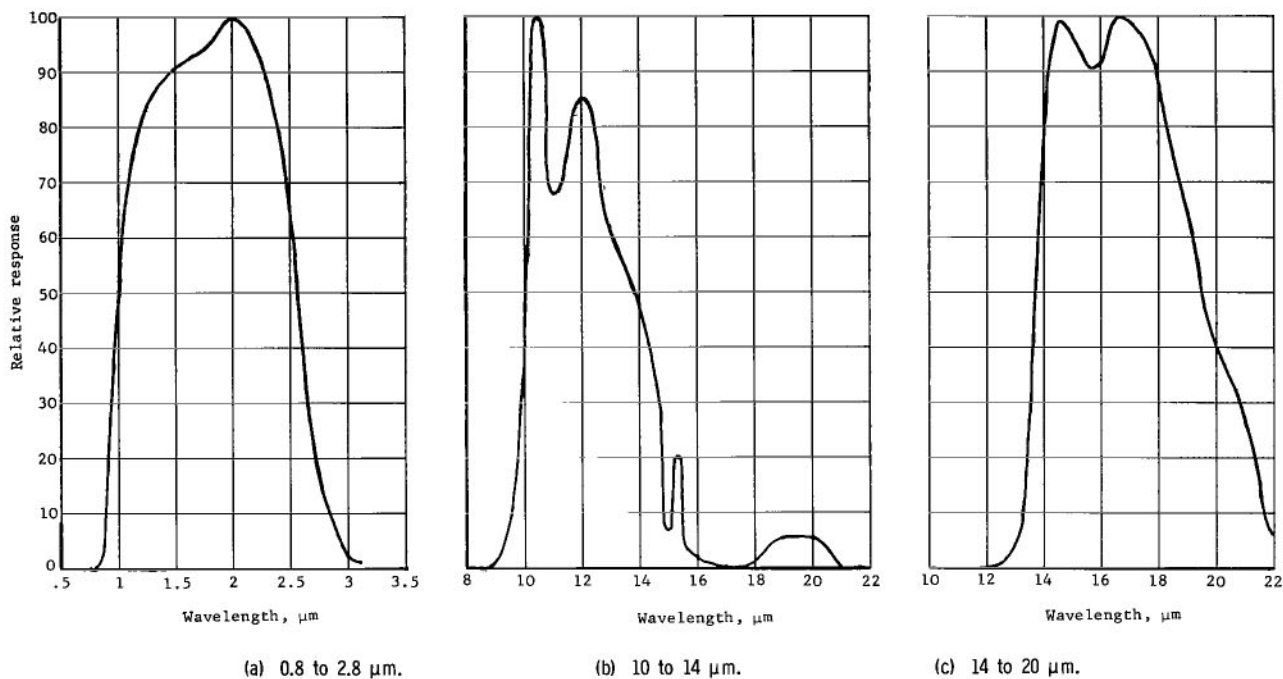


Figure 6.- Radiometer spectral-response curves for each flight.

and the temperature and pressure distributions along the line of sight. Because a spherically stratified atmosphere is assumed in the calculations for mathematical simplicity, the construction of a model atmosphere consists of the specification of temperature and mixing ratio as functions of pressure altitude. (See ref. 3.) The model atmospheres derived for this purpose are listed in tables II, III, and IV. The methods used to derive these atmospheres and the meteorological measurements employed are described in appendix C.

The theoretical infrared horizon profiles for the 10 to 14 μm and 14 to 20 μm spectral intervals (corresponding to flights 2 and 3, respectively) were computed by J. Alishouse of the National Environmental Satellite Center of the Environmental Science Services Administration (ESSA) by using the ESSA infrared radiance calculation program (ref. 3). The profile for the 0.8 to 2.8 μm spectral interval was obtained from reference 5.

FLIGHT-TEST RESULTS

Several of the radiance profiles which were measured in the three spectral intervals are listed in tables V to VII. The radiance profiles, together with the respective cloud charts, are shown in figures 7 to 12. The measured radiance profiles are compared with theoretical profiles based on the meteorological conditions existing at the time of each flight. The radiance values of the horizon profiles presented in this paper are given in terms of effective radiance. To compare the actual values of radiance from the horizon with those shown, the actual values must be multiplied by the radiometer optical filter response. An estimate of the accuracy of the measurements can be obtained from appendix D.

Flight 1

Flight 1, which was conducted on July 8, 1964, obtained horizon-profile measurements in the 0.8 to 2.8 μm spectral interval. The primary radiant energy in this wavelength interval is reflected and scattered solar energy, as shown by curve A in figure 13. The scattering particles include air molecules and atmospheric aerosols, such as dust, smoke, salts, and water. The amount of scattered energy received by the sensor depends strongly on the angle between sensor line of sight and the direction of solar illumination, as well as on the wavelength of the radiation, and size, type, and density of the particles.

Several of the radiance profiles measured during flight 1 are given in table V and figure 7. The solid-line curve in figure 7 is a smoothed profile obtained by averaging the measured radiance of all horizon crossings at each tangent height. The cross-hatched area about this curve represents the envelope containing all data, and the dotted curve is typical of the measured profiles obtained.

Figure 7 shows that sunlight scattered by the atmosphere causes a smooth increase in the energy received by the radiometer as its line of sight sweeps from a tangent height of 50 to 20 km. A steep increase in radiance occurs slightly below a tangent height of 20 km and leads to a plateau which extends to a tangent height of approximately 12 km. This feature is apparent in the curve representing a typical horizon profile but is subdued in the average curve because of variation in altitudes between individual profiles. This energy can be explained by solar radiation scattered by one or several aerosol constituents which surround the earth at altitudes of approximately 14 km and 19 km, and which are invisible from the earth's surface because they have little optical thickness in the vertical direction (ref. 6).

Below a tangent height of 10 km the profile is dominated by energy from cirrus clouds which covered the area of earth where the profiles were obtained. Successive clouds can be noted at tangent altitudes of 10 km and -1 km for the typical horizon

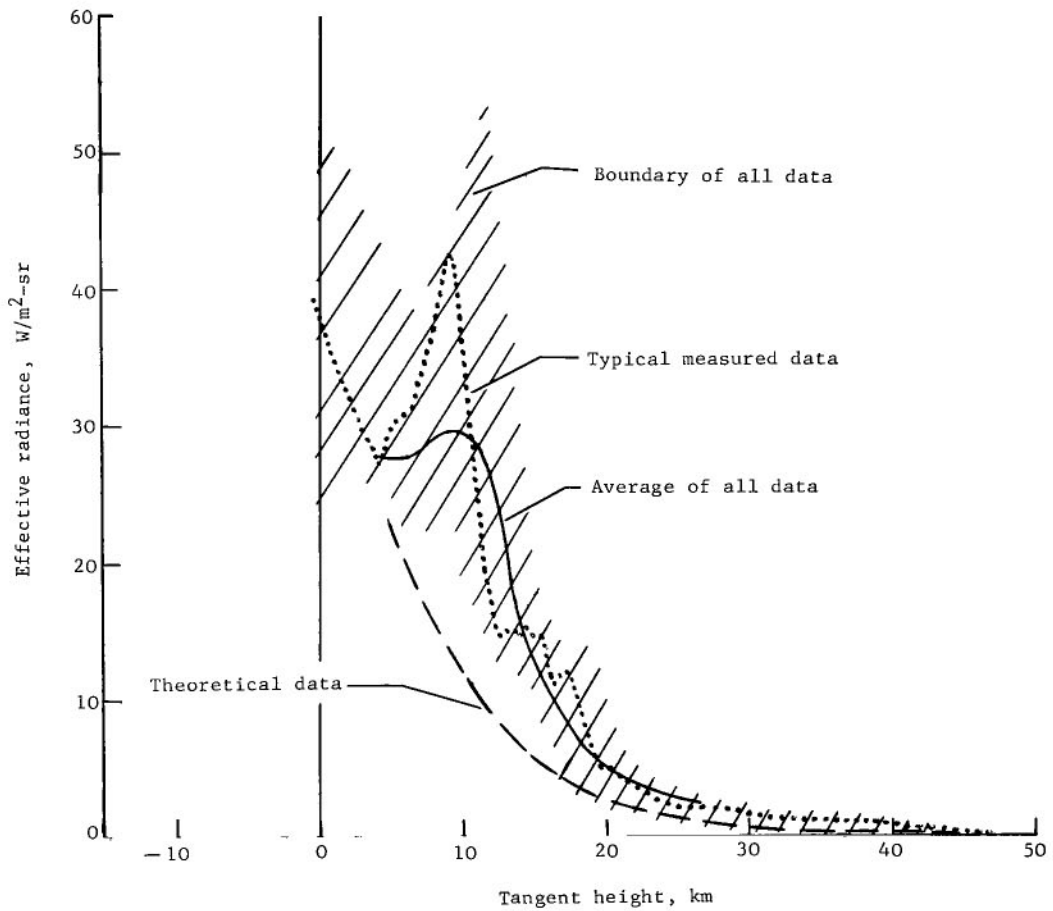


Figure 7.- The 0.8 to 2.8 μm horizon radiance profile. Flight 1; July 8, 1964; observer altitude, 50.3 km.

crossing shown in figure 7. The clouds as detected by the radiometer are consistent with the conditions shown by the 16-mm motion-picture camera mounted next to the radiometer and by the weather patterns existing that day as shown in figure 8. The dashed-line box in figure 8 shows the area where the horizon crossings were obtained. The area of view was partly clear but high cirrus clouds covered much of the sky to the east. The maximum measured effective radiance shown in figure 7 is $52 \text{ W/m}^2\text{-sr}$. The solar energy which the radiometer would measure when looking at clouds with an albedo of 1 is $94.5 \text{ W/m}^2\text{-sr}$, so that the measured effective radiance corresponds to an albedo of $\frac{52}{94.5} = 0.55$ which compares favorably with available data.

Figure 7 also shows the theoretical horizon profile for primary Rayleigh scattering (ref. 5). This profile applies to the northern horizon toward which the radiometer was pointing. The measured data indicate that more solar energy is scattered toward the observer than the theoretical curve predicts. Because calculations were limited to primary molecular scattering, the higher energy reaching the radiometer can be accounted for by multiple scattering and the presence of aerosols.

The results of tests in the near infrared region indicate that the 0.8 to $2.8 \mu\text{m}$ interval is not a good region for horizon sensors. The radiance above a tangent height of 20 km results from scattering. The gradient in this region is shallow and, as noted in the measured results, it is variable because of multiple scattering, varying aerosol content, and small changes in sun angle. Between 15 km and 20 km , the gradient is steeper but the variance in the boundaries of the data increases. Below a tangent height of 15 km the gradient is very steep, but clouds are extremely variable; therefore, this region does not possess the qualities of a steep invariant radiance profile.

Flight 2

Figure 13 shows that beyond $4.6 \mu\text{m}$ a horizon sensor in space would receive radiation mainly from the earth and its atmosphere. Therefore, a horizon sensor which operates in a spectral interval in the far infrared region can sense the horizon on the dark (night) side as well as the sunlit (day) side of the earth and is virtually independent of the sun's position.

For a far infrared sensor which includes no, or at most weak, atmospheric absorption bands within its spectral region, the sensor receives its radiant energy from opaque bodies, such as the earth itself, or from clouds that may screen it. The amount of radiance received by such a sensor from the earth for clear conditions (curve B of fig. 13) differs greatly from that received from clouds for overcast conditions (curve D of fig. 13) and, therefore, a strong dependence on meteorological conditions is implied. The spectral interval from 10 to $14 \mu\text{m}$ is an example of a window region where atmospheric absorption is low.

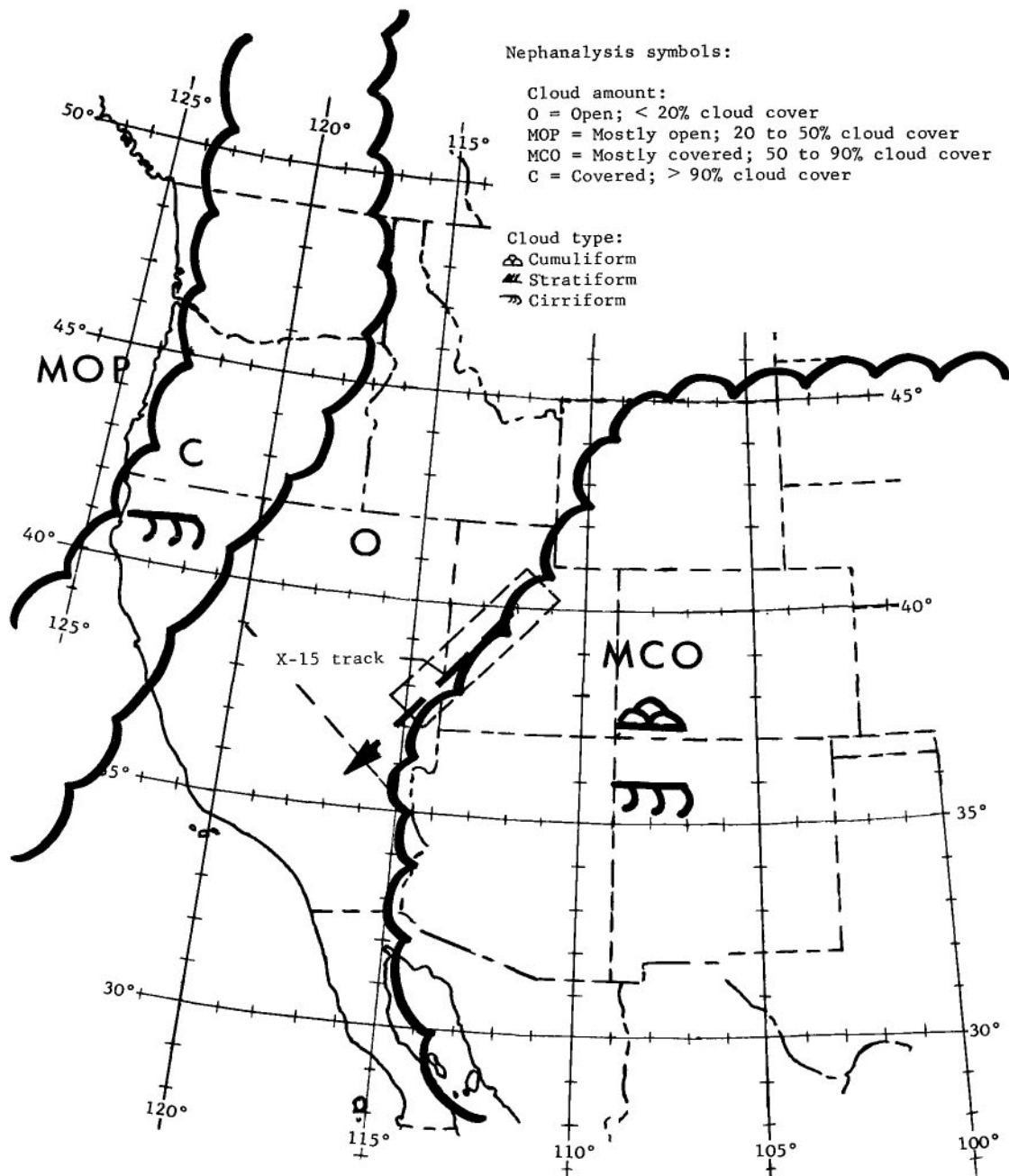


Figure 8.- Nephanalysis (cloud chart) for 0.8 to 2.8 μm spectral interval. Flight 1; 00:00 GMT, July 9, 1964.

Flight 2 was made on May 28, 1965, and measured the earth's horizon profile in this spectral interval. The data are shown in figure 9 where the solid curve is the averaged radiance profile as previously described. Other measured radiance profiles, which are all within the cross-hatched area, are given in table VI. The dashed curve is a theoretical profile calculated by ESSA for the 10 to 14 μm radiometer spectral response shown in figure 6(b) and from the meteorological data for flight 2. The measurements were obtained in an almost clear and cloudless area, as shown in figure 10, and represent the most favorable conditions for this spectral interval. The radiometer spectral response (fig. 6(b)) must be considered when discussing the profiles shown in figure 9 because atmospheric absorption bands exist at each end of the spectral region. A carbon dioxide absorption band centered at 15 μm extends to about 12 μm . Energy from this band, along with radiation from ozone in two of its bands at 9.6 μm and 14.08 μm , accounts for the slow increase in radiance at tangent heights from 50 to 15 km. This feature of the profile is evident in both the measured data and the theoretical profile calculated for the conditions existing during the data period. When the radiometer line of sight sweeps to a tangent height of about 5 km, the instrument receives radiation from dust and haze present at low altitudes. When the field of view contains the earth, blackbody radiation from it is also received.

The relatively smooth increase in all radiance profiles below a tangent height of 0 km indicates that no clouds came within the field of view of the radiometer. This result agrees with the nephanalysis shown in figure 10 which showed few clouds over the region of coverage.

According to the profiles, the 10 to 14 μm interval appears to be well suited for horizon sensing because the gradient between 0 km and 10 km is steep and reasonably invariant. However, in this interval the presence of clouds could cause extreme variations in radiance level. Hence, while it can be concluded that the 10 to 14 μm spectral interval offers excellent possibilities for use of horizon sensors in clear weather, it has been shown analytically (ref. 2) that the effects of low-altitude weather variations make it of doubtful value for general use.

Flight 3

For a far infrared sensor whose spectral response is contained entirely within a strong atmospheric absorption band, the radiant energy received is primarily thermal radiation from the atmospheric gas. In practice, a combination of thermal radiation from the atmospheric gas and from the earth or clouds below it is usually obtained because the gas is not totally opaque. The selection of a spectral interval which contains a strong atmospheric absorption band results in shielding the earth and cloud surfaces by the emission from the high-altitude atmospheric gases and, thus, in minimizing the effects of variable cloud conditions.

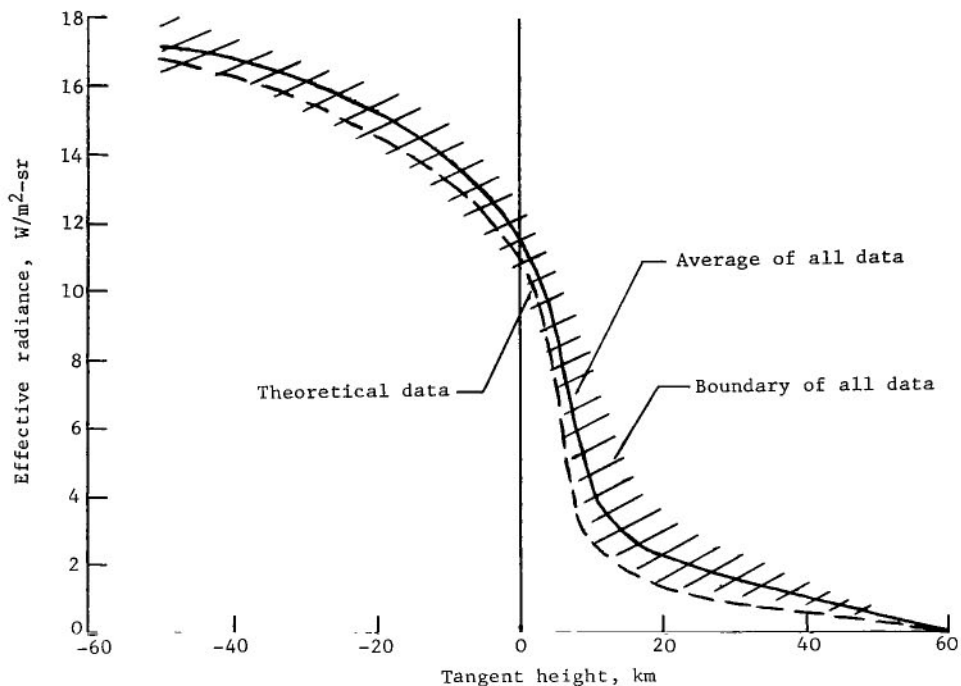


Figure 9.- The 10 to 14 μm horizon radiance profile. Flight 2; May 28, 1965; observer altitude, 62 km.

Carbon dioxide, water vapor, and ozone have absorption bands in the infrared spectrum and radiate electromagnetic energy in the spectral intervals where they absorb. (See refs. 5 and 7 for a more complete discussion of the radiation characteristics of the atmosphere.) Of course, the thermal radiation depends on the temperature of the gas in question and, consequently, on altitude as indicated in figure 7. For a given pointing direction of the radiometer, the optical path from which energy is received can be determined. The effective mass of absorbing gas in the path can be found if the pressure and mixing ratios of the gases are known. The power radiated by the gas in the spectral interval of the sensor can then be determined from Planck's equation if the temperature of the gas is also known. The total energy received by the sensor is found by summing the gas radiation from each portion of the optical path, while correcting for the attenuation by absorption between the radiating point and the sensor. If the optical path is intercepted by an opaque body such as a cloud or the earth, the attenuated radiation from the body must also be included. A detailed discussion of this procedure is given in reference 2.

Figure 11 shows the radiance profile obtained in the 14 to 20 μm interval. The solid curve is the averaged radiance profile as described for figure 7. The radiance elements in this region between 14 μm and 16 μm are CO_2 and in the neighborhood of 18 μm to beyond equipment cutoff are rotational H_2O .

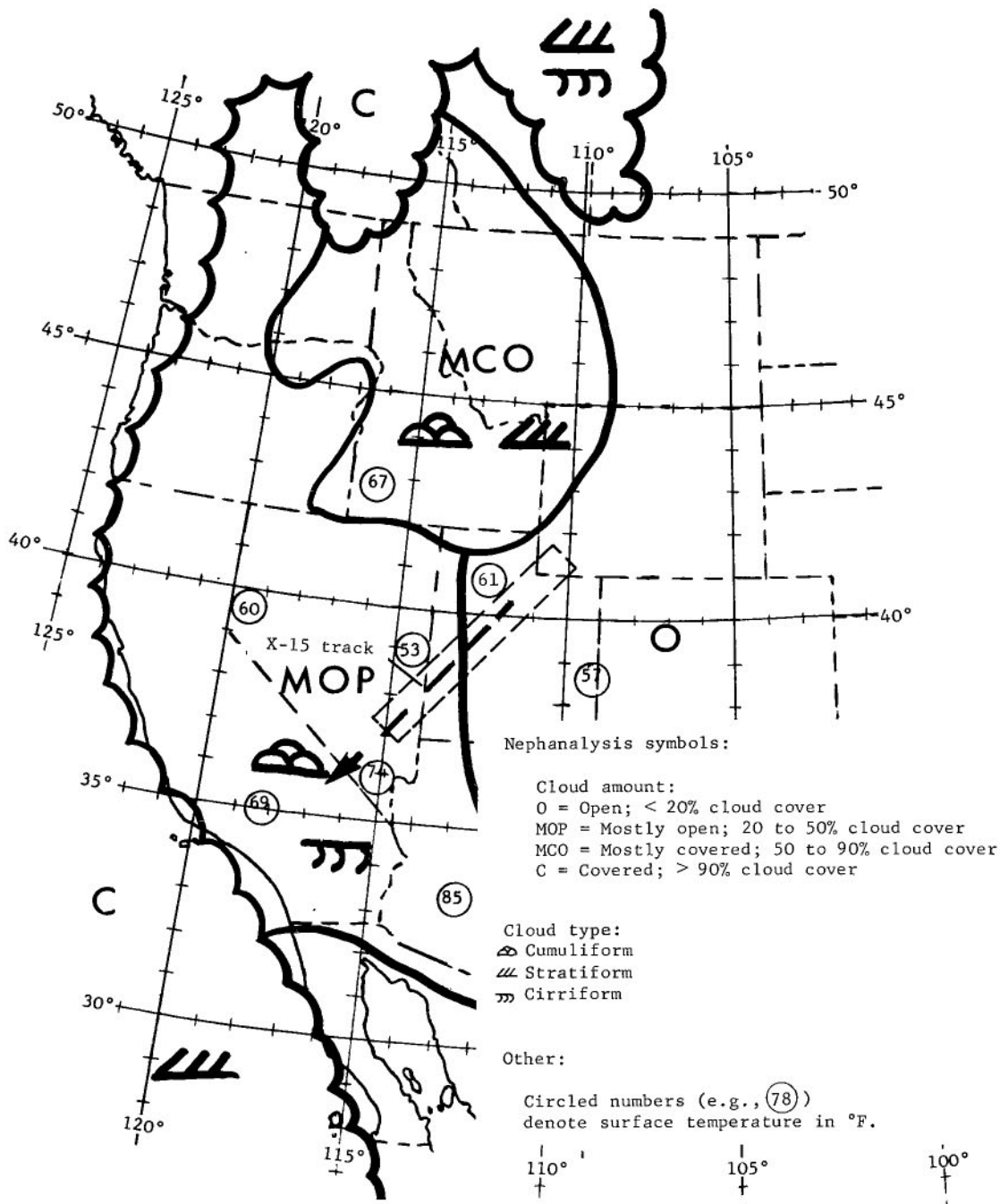


Figure 10.- Nephanalysis (cloud chart) for 10 to 14 μ m spectral interval. Flight 2; 18:00 GMT, May 28, 1965.

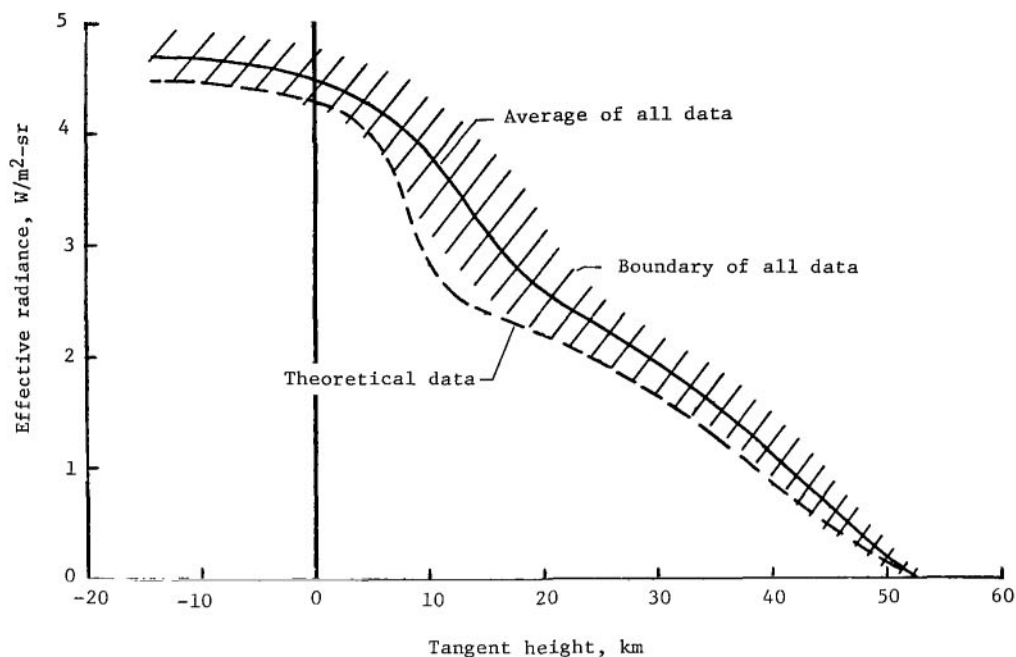


Figure 11.- The 14 to 20 μm horizon radiance profile. Flight 3; June 29, 1965; observer altitude, 76 km.

Because the amount of water vapor in the upper atmosphere beyond 25 km is small, most of the radiation in this region is due to CO_2 . The CO_2 region is thought to be a most desirable region because the mixing ratio is constant and the absorptivity is great enough to screen out the lower atmospheric variability due to weather phenomena.

The comparison between the results above a tangent height of 25 km shows good agreement between theory and measurement and the boundary of all the measurements shows the smallest variation of any spectral region measured. The boundary is within the ± 4 -km uncertainty due to the position and radiance error of the experiment. The gradient in this range is steep and thus indications are that the 14 to 16 μm interval is usable for horizon sensors.

The measurements for tangent heights below 20 km show more variability and somewhat less agreement with theory. The average water-vapor mixing ratio can be estimated for a relatively large area but is harder to predict exactly for any specific locality. This uncertainty can account for the wider divergence and also the greater scatter in the measured data. In addition, some clouds were indicated by the motion pictures but were not observed in the measured radiance profiles. These clouds must have been widely scattered as indicated by the nephelometry of figure 12. This disagreement also indicates variability in water-vapor mixing ratio on a local level.

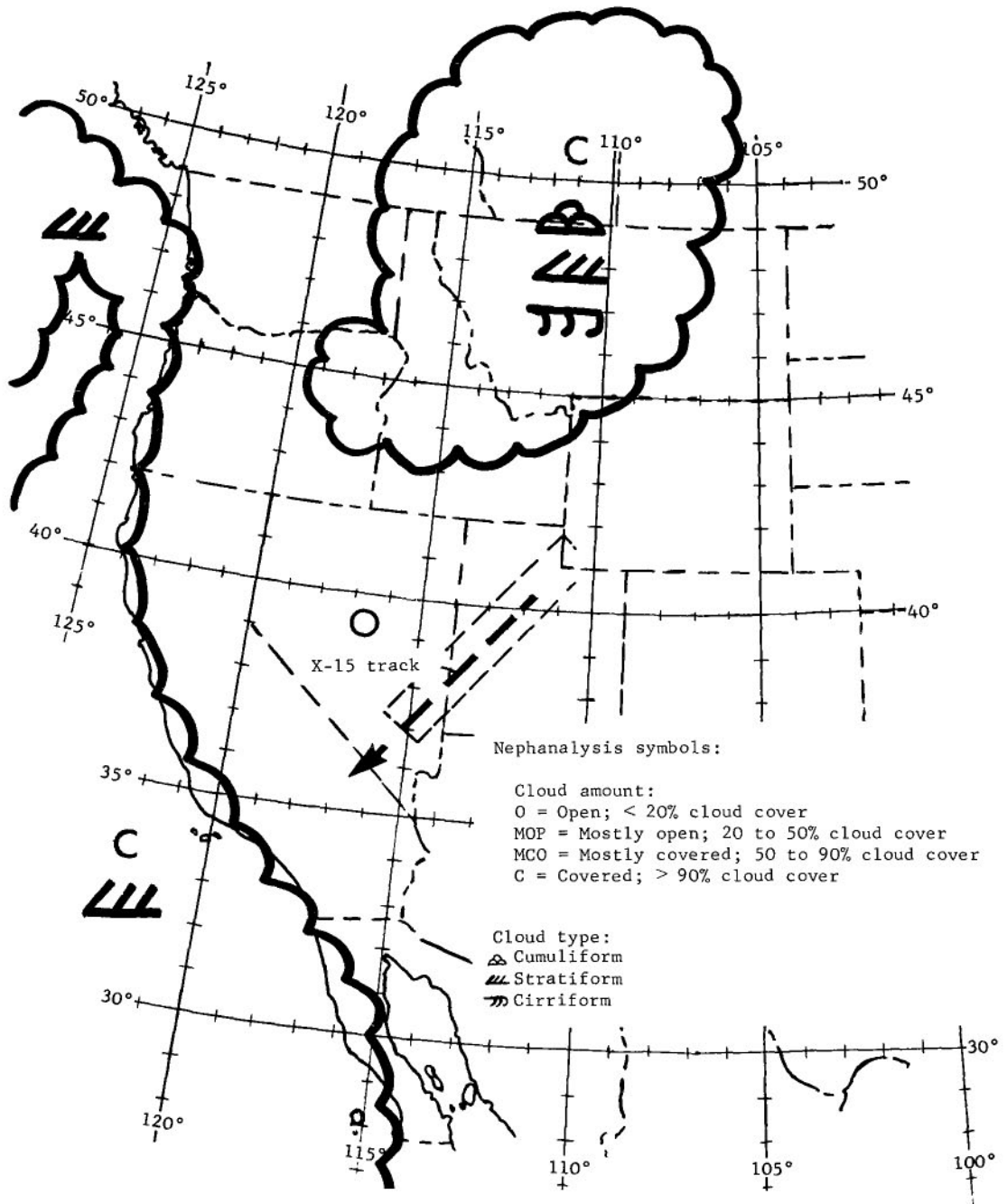


Figure 12.- Nephanalysis (cloud chart) for 14 to 20 μm spectral interval. Flight 3; 18:00 GMT, June 29, 1965.

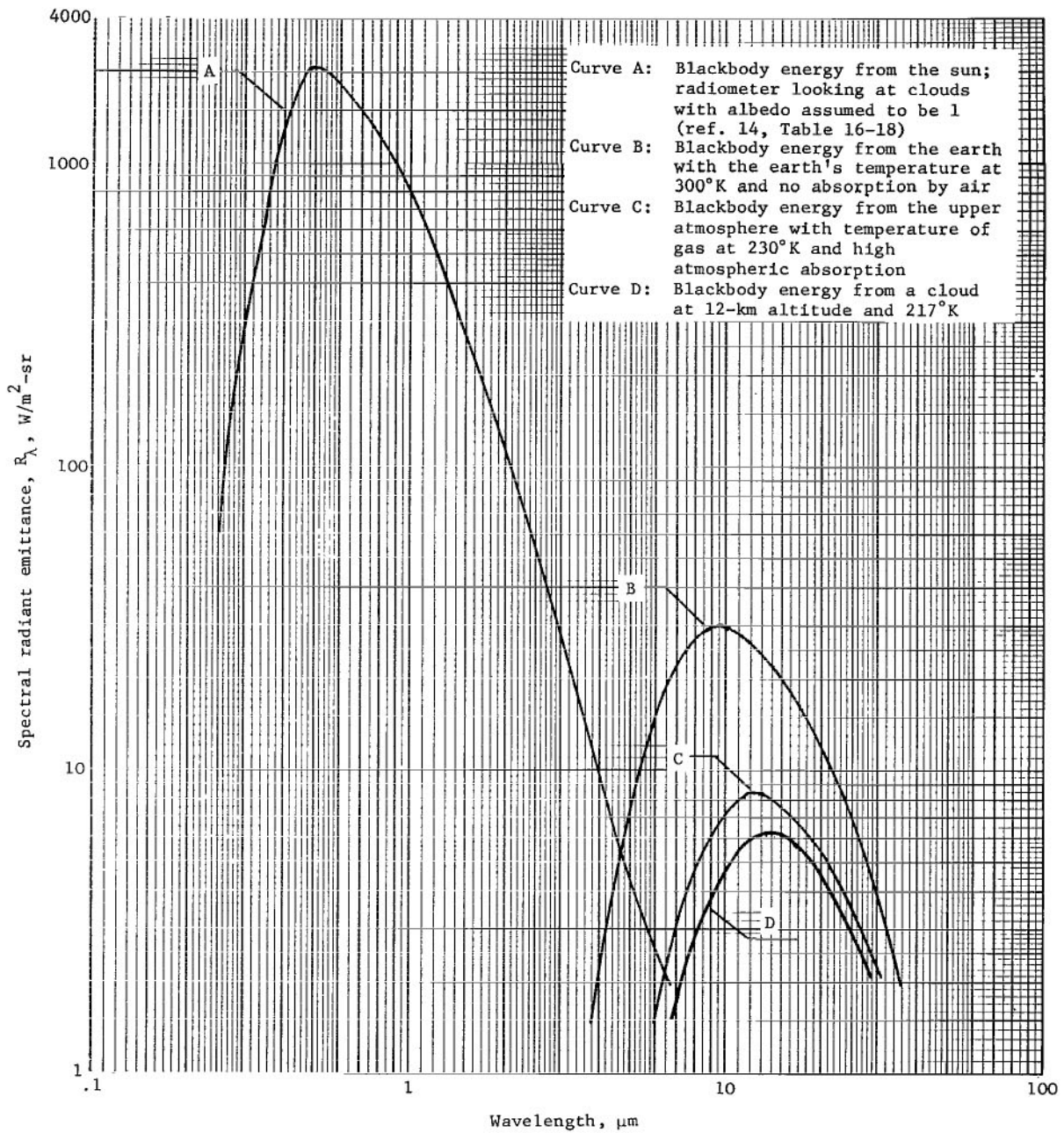


Figure 13.- Spectral radiant emittance of several sources seen by radiometer outside earth's atmosphere.

CONCLUSIONS

Experimental data of the earth's horizon in three spectral intervals have been obtained. The resolution (field of view) of the data at the tangent point is approximately 2 km, and the spatial position of the horizon profile is known to within 4 km.

The 14 to 20 μm interval was shown to be the best spectral interval for horizon sensing because it exhibits the least variance at adequate radiant intensity. The 0.8 to 2.8 μm and 10 to 14 μm spectral intervals do not appear suitable for accurate horizon sensing because they are sensitive to low-altitude meteorological changes.

The experimental data obtained verified the theory used to predict, within experimental accuracy, the far infrared radiant energy due to carbon dioxide. The use of theory for spectral regions where high-altitude water-vapor data are required is questionable because no mixing-ratio information is available. The primary scattering theory cannot predict accurately the radiant energy in the near infrared region ($<3.0 \mu\text{m}$).

The X-15 airplane provides a convenient test bed for programs requiring high altitudes and altitude and position data. Also, good weather data are available for the points viewed by the radiometer.

Langley Research Center,
National Aeronautics and Space Administration,
Langley Station, Hampton, Va., March 15, 1968,
715-02-00-01-23.

APPENDIX A

DERIVATION OF THE EXPRESSION RELATING TANGENT HEIGHT TO MEASURED PARAMETERS

In this section the equation expressing tangent height as a function of known flight parameters will be developed. It is helpful to define four primary coordinate systems: a space-fixed coordinate system, an aircraft coordinate system, a radiometer coordinate system, and a local earth coordinate system. The space-fixed coordinate is defined to have an x_S -axis positive south, a y_S -axis positive west, and a z_S -axis positive downward. The aircraft coordinate system, which is assumed to be initially aligned with the space-fixed coordinate system, has an x_a -axis positive in the direction of the aircraft nose, a y_a -axis positive along the right wing, and a z_a -axis positive downward. The radiometer has its x_R -axis in the scan plane of the radiometer line of sight, its y_R -axis in the direction of the right wing of the X-15 and lying in the plane of the aircraft x_a and y_a body axes, and a z_R -axis completing the right-hand triad. The local earth coordinate system consists of an x -axis positive south, a y -axis positive east, and a z -axis directed along the local vertical, positive upward.

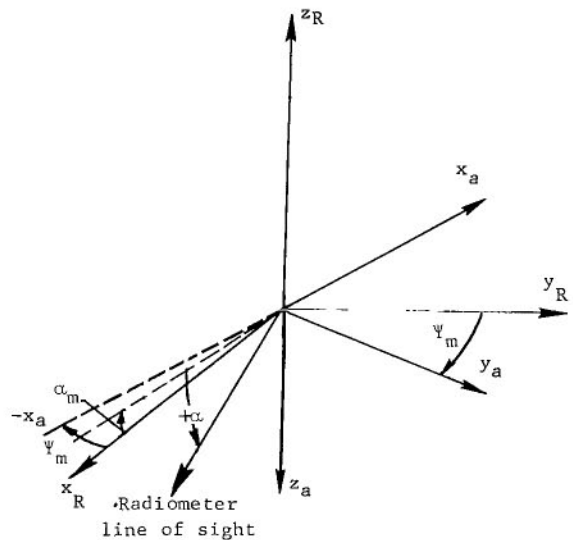


Figure 14.- Radiometer orientation in X-15.

The scan angle of the radiometer, the pitch mounting angle, and the yaw mounting angle must be considered to be transformations, as shown in figure 14. In this figure ψ_m is a positive Euler rotation in the direction shown. The α rotation is a positive Euler angle in the direction shown and α_m is a negative angle as described. The line-of-sight vector, a unit vector initially along the x_R -axis, can be described by

$$\begin{bmatrix} x_R \\ y_R \\ z_R \end{bmatrix} = \begin{bmatrix} x_R \\ 0 \\ 0 \end{bmatrix} = \begin{bmatrix} 1 \\ 0 \\ 0 \end{bmatrix} \quad (A1)$$

The transformation matrices which define the rotations ψ_m , α , and α_m are then

APPENDIX A

$$M_1 = \begin{bmatrix} \cos \psi_m & -\sin \psi_m & 0 \\ \sin \psi_m & \cos \psi_m & 0 \\ 0 & 0 & 1 \end{bmatrix} \begin{bmatrix} \cos(\alpha + \alpha_m) & 0 & \sin(\alpha + \alpha_m) \\ 0 & 1 & 0 \\ -\sin(\alpha + \alpha_m) & 0 & \cos(\alpha + \alpha_m) \end{bmatrix} \quad (A2)$$

The alinement of the radiometer coordinates with the aircraft coordinates can be accomplished by the following transformation matrix:

$$M_2 = \begin{bmatrix} -1 & 0 & 0 \\ 0 & 1 & 0 \\ 0 & 0 & -1 \end{bmatrix} \quad (A3)$$

Therefore,

$$\begin{bmatrix} x_a \\ y_a \\ z_a \end{bmatrix} = [M_2] [M_1] \begin{bmatrix} x_R \\ y_R \\ z_R \end{bmatrix} \quad (A4)$$

or

$$\begin{bmatrix} x_a \\ y_a \\ z_a \end{bmatrix} = \begin{bmatrix} -1 & 0 & 0 \\ 0 & 1 & 0 \\ 0 & 0 & -1 \end{bmatrix} \begin{bmatrix} \cos \psi_m & -\sin \psi_m & 0 \\ \sin \psi_m & \cos \psi_m & 0 \\ 0 & 0 & 0 \end{bmatrix} \begin{bmatrix} \cos(\alpha + \alpha_m) & 0 & \sin(\alpha + \alpha_m) \\ 0 & 1 & 0 \\ -\sin(\alpha + \alpha_m) & 0 & \cos(\alpha + \alpha_m) \end{bmatrix} \begin{bmatrix} 1 \\ 0 \\ 0 \end{bmatrix} \quad (A5)$$

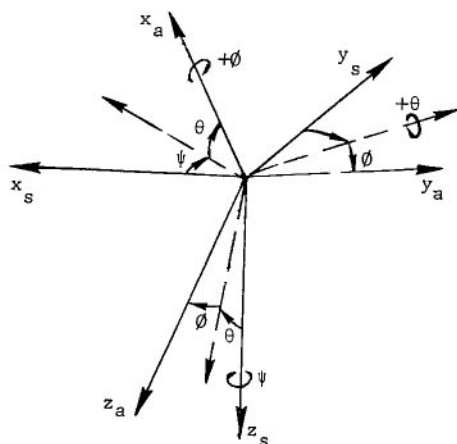


Figure 15.- Order of rotation through attitude angles.

The angular relationships between aircraft coordinates and space coordinates are the stable platform parameters, roll, pitch, and yaw. The ordered rotations indicated in equation (A5) are used to define aircraft coordinates in terms of space coordinates. However, it is desired to define space coordinates in terms of aircraft coordinates so that the inverse relationships must be used. If yaw, pitch, and roll are designated by ψ , θ , and ϕ , respectively, in figure 15, and if the directions of rotation are positive as shown and represent the ordered rotation necessary to transform space coordinates into aircraft coordinates, the space coordinates are found by the following transformation:

APPENDIX A

$$\begin{bmatrix} x_s \\ y_s \\ z_s \end{bmatrix} = [\psi][\theta][\phi] \begin{bmatrix} x_a \\ y_a \\ z_a \end{bmatrix} = M_3 \begin{bmatrix} x_a \\ y_a \\ z_a \end{bmatrix} \quad (A6)$$

where

$$[\psi] = \begin{bmatrix} \cos \psi & -\sin \psi & 0 \\ \sin \psi & \cos \psi & 0 \\ 0 & 0 & 1 \end{bmatrix} \quad (A7)$$

$$[\theta] = \begin{bmatrix} \cos \theta & 0 & \sin \theta \\ 0 & 1 & 0 \\ -\sin \theta & 0 & \cos \theta \end{bmatrix} \quad (A8)$$

$$[\phi] = \begin{bmatrix} 1 & 0 & 0 \\ 0 & \cos \phi & -\sin \phi \\ 0 & \sin \phi & \cos \phi \end{bmatrix} \quad (A9)$$

Substitution of equation (A4) into equation (A6) yields

$$\begin{bmatrix} x_s \\ y_s \\ z_s \end{bmatrix} = [M_3][M_2][M_1] \begin{bmatrix} 1 \\ 0 \\ 0 \end{bmatrix} \quad (A10)$$

The single transformation which will cause the space-fixed and local earth coordinate systems to become coincident is represented by

$$M_4 = \begin{bmatrix} 1 & 0 & 0 \\ 0 & -1 & 0 \\ 0 & 0 & -1 \end{bmatrix} \quad (A11)$$

Thus, the total transformation which is obtained by combining equations (A10) and (A11) is

$$\begin{bmatrix} x \\ y \\ z \end{bmatrix} = [M_4][M_3][M_2][M_1] \begin{bmatrix} 1 \\ 0 \\ 0 \end{bmatrix} \quad (A12)$$

APPENDIX A

Multiplying matrices in equation (A12) yields the direction of the radiometer line of sight in local coordinates as follows:

$$\begin{bmatrix} x_R \\ y_R \\ z_R \end{bmatrix} = \begin{bmatrix} \cos \psi \left\{ -\cos \theta \cos \psi_m \cos(\alpha + \alpha_m) + \sin \theta \left[\sin \phi \sin \psi_m \cos(\alpha + \alpha_m) + \cos \phi \sin(\alpha + \alpha_m) \right] \right\} - \sin \psi \left[\cos \phi \sin \psi_m \cos(\alpha + \alpha_m) - \sin \phi \sin(\alpha + \alpha_m) \right] \\ -\sin \psi \left\{ -\cos \theta \cos \psi_m \cos(\alpha + \alpha_m) + \sin \theta \left[\sin \phi \sin \psi_m \cos(\alpha + \alpha_m) + \cos \phi \sin(\alpha + \alpha_m) \right] \right\} - \cos \psi \left[\cos \phi \sin \psi_m \cos(\alpha + \alpha_m) - \sin \phi \sin(\alpha + \alpha_m) \right] \\ -\sin \theta \cos \psi_m \cos(\alpha + \alpha_m) - \cos \theta \left[\sin \phi \sin \psi_m \cos(\alpha + \alpha_m) + \cos \phi \sin(\alpha + \alpha_m) \right] \end{bmatrix} \quad (A13)$$

The direction cosine of the line of sight (fig. 1) is given by

$$\cos \beta = (-z \text{ component of line of sight})$$

or

$$\cos \beta = \sin \theta \cos \psi_m \cos(\alpha + \alpha_m) + \cos \theta \left[\sin \phi \sin \psi_m \cos(\alpha + \alpha_m) + \cos \phi \sin(\alpha + \alpha_m) \right] \quad (A14)$$

From figure 1, it follows that

$$\sin \beta = \frac{h + r}{h_{X-15} + r} \quad (A15)$$

Solving for h gives

$$h = (h_{X-15} + r) \sin \beta - r \quad (A16)$$

APPENDIX A

where β is obtained from equation (A14). Substituting the expression for β into equation (A16) gives

$$h = \left[\sin \left(\cos^{-1} \left\{ \sin \theta \cos \psi_m \cos(\alpha + \alpha_m) + \cos \theta \left[\sin \phi \sin \psi_m \cos(\alpha + \alpha_m) + \cos \phi \sin(\alpha + \alpha_m) \right] \right\} \right) \right] (h_{X-15} + r) - r \quad (\text{A17})$$

APPENDIX B

RADIOMETER DESIGN AND CALIBRATION

This appendix gives a more detailed description of the radiometer design parameters and of a method used to correct the measured data for the radiometer frequency response, as well as a description of the radiometer calibration.

The smallest obtainable field of view, which determines maximum data resolution, is dictated by the resolution limit of the optics and the detectivity of available detectors. By using Rayleigh's criterion, for the 12.7-cm aperture of the X-15 radiometer and the shortest wavelength considered ($\lambda \approx 1.0 \mu\text{m}$), the diffraction-limited resolution is

$$\theta_R = 1.22 \frac{\lambda}{D} \times 57.3 = 5.52 \times 10^{-4} \text{ deg} \quad (\text{B1})$$

Because it is almost impossible to produce diffraction-limited optics with an f-number of 1, it must be expected that aberrations degrade this resolution. In addition, the flat optical filter in the converging beam further degrades the resolution, inasmuch as rays incident at different angles from the normal will come to focus at slightly varying focal lengths. Resolution tests of the flight optics using visible light at finite and infinite distances yielded a telescope resolution estimate of 0.03° . The detector size was selected to yield a field of view of 0.13° by 0.13° at the half-response points so that resolution is largely determined by the detector. The spectral response of the radiometric systems as a function of wavelength for each mission is shown in figure 6. The optical filter and detector response were measured separately, multiplied, and corrected for scan and objective mirror reflectance to yield the curves in figure 6.

Detector and Electronics

The detector subsystems of the radiometer for each mission are somewhat different. The characteristics of the three systems are given in table I; however, the parameters for only one system (flight 1) will be derived to illustrate the approach used to generate the table. The equipment used in flight 1 operated in the 0.8 to 2.8 μm interval and the detector was an uncooled lead sulfide photoconductive cell. Its response combined with that of the optical filter gives the overall radiometer response as shown in figure 6. The noise equivalent power (NEP) of the detector, in $\text{W}/\text{Hz}^{1/2}$, or the root-mean-square value of the radiant energy flux, in watts, necessary to give a signal-to-noise ratio of unity, is defined as (ref. 7) $\frac{H A V_N}{V_S(\Delta f)^{1/2}}$. For the 0.8 to 2.8 μm interval at a source temperature of 500°K , at a chopping speed of 15 Hz, and with an equivalent noise bandwidth of 1 Hz, the NEP was measured to be $2.07 \times 10^{-11} \text{ W}/\text{Hz}^{1/2}$. The electrical bandpass of the

APPENDIX B

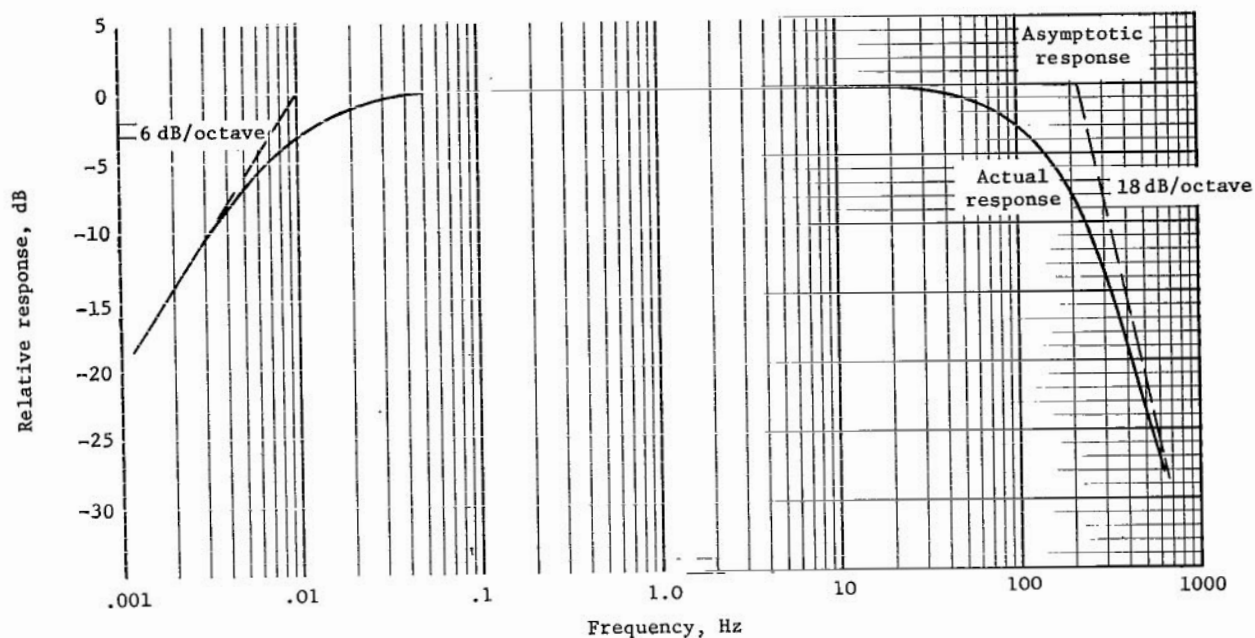


Figure 16.- Transfer function of 0.8 to 2.8 μm radiometer electronics.

radiometer system electronics is shown in figure 16. The equivalent noise bandwidth is defined as (ref. 8)

$$B = \frac{1}{K^2} \int_0^{\infty} |G(j\omega)|^2 d\omega \quad (\text{B2})$$

where $G(j\omega)$ is the transfer function of the system and K is the midband gain of $G(j\omega)$. For the transfer function shown in figure 16,

$$B = \frac{3\pi}{16} 220 = 130 \text{ Hz} \quad (\text{B3})$$

For $T = 500^\circ \text{K}$, $f_c = 15 \text{ Hz}$, and $B = 130 \text{ Hz}$, the NEP is equal to $2.37 \times 10^{-10} \text{ W/Hz}^{1/2}$. The quality of the radiometer may be expressed independently of area by its detectivity, given as

$$D^* = \frac{A_{\text{detector}}^{1/2}}{\text{Noise equivalent power}} \quad (\text{B4})$$

The noise bandwidth is always taken to be 1 Hz. Then the detectivity for the near infrared radiometer is $1.45 \times 10^9 \text{ cm-Hz}^{1/2}/\text{W}$.

The detector is connected in a bridge circuit as shown in figure 17. The active cell is exposed to the radiant flux received by the radiometer, while the compensator cell is completely shielded from radiant energy. Two cells are selected whose electrical

APPENDIX B

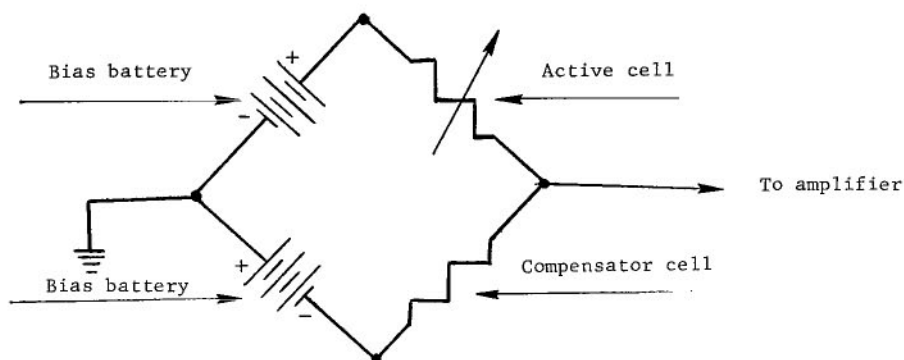


Figure 17.- Detector bridge circuit.

characteristics are matched, and both are mounted in close thermal proximity. Gross dc unbalance due to changes in ambient temperature is thus eliminated because both legs of the bridge change by the same amount. However, because perfectly matched detectors are not available, ambient-temperature variations during flight are sufficient to result in dc offsets comparable to the radiometric signal output. To filter out these unwanted low-frequency signals, the amplifier uses ac coupling, with the low-frequency breakpoint at 0.01 Hz. A second advantage of using ac coupling is noise filtering, since a large part of the noise generated in the detector is current noise, which has an intensity variation roughly inversely proportional to frequency. The limiting consideration on the choice of low-frequency cutoff is dictated by the amount of distortion to the data due to excessive droop.

Because the primary goal of the program is to measure and compare theoretical and experimental radiance profiles, the effect of the electronic system must be accounted for in the measured radiance. The method for estimating the effect of ac coupling and the equivalent electronic-system time delay is discussed in the following paragraphs.

Figure 18 which gives an assumed trapezoidal radiance input to the radiometer as a function of time shows the effect of amplifier time response. Also shown is the radiometer output waveform for the assumed radiance input. Because of the electronic frequency response the output lags behind the input, the output signal does not reach full amplitude, and for constant input the output decays to zero. The severity of these factors is determined by the low- and high-frequency cutoffs of the system. During data reduction the amount of droop that occurs during a horizon crossing must be removed from the record. Because the input forcing function is zero while the radiometer looks at space, an exponential decay of the amplifier output results. Because superposition holds, the exponential

APPENDIX B

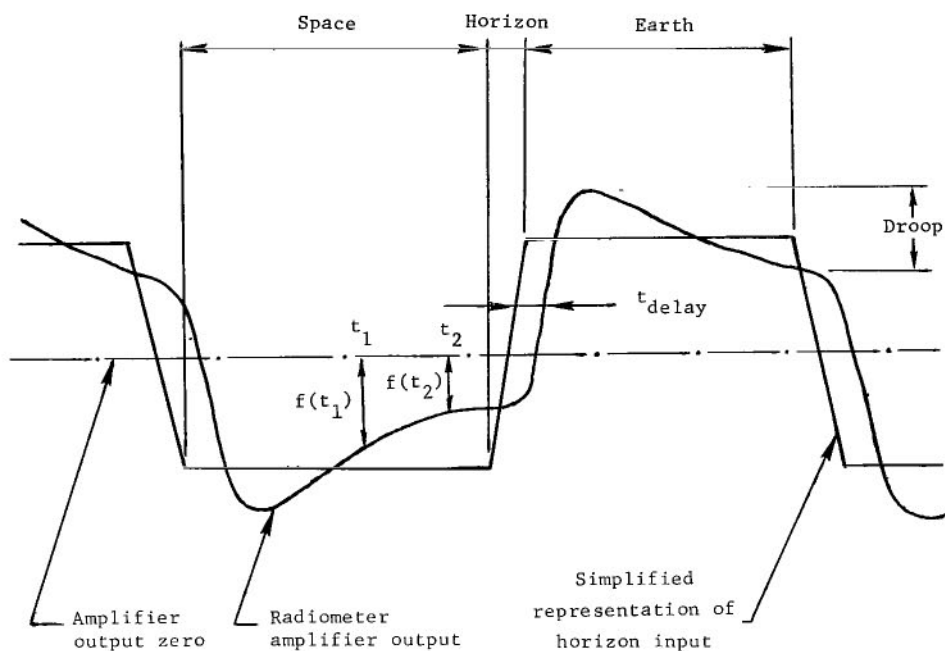


Figure 18.- Effect of amplifier time response.

can be extrapolated through the time of the horizon crossing and its effect removed from the recorded signal. Therefore, the correction can be made especially well for those profiles where the radiometer line of sight sweeps from space to earth.

The following procedure can be used to allow for extrapolation of the exponential. The amplitude $f(t_1) - f(t_2)$ and the time $t_1 - t_2$ can be measured as indicated in figure 18. Because the amplifier has a single low-frequency time constant the output functions for space input at t_1 and t_2 are

$$f(t_1) = V_i \epsilon^{-t_1/\tau} \tag{B5}$$

$$f(t_2) = V_i \epsilon^{-t_2/\tau} \tag{B6}$$

Multiplying equation (B6) by $\epsilon^{t_1/\tau} \epsilon^{-t_1/\tau}$ gives

$$f(t_2) = V_i \epsilon^{(t_1-t_2)/\tau} \epsilon^{-t_1/\tau} \tag{B7}$$

If $\epsilon^{(t_1-t_2)/\tau} = K$,

$$f(t_2) = Kf(t_1) \tag{B8}$$

APPENDIX B

Hence,

$$f(t_1) - f(t_2) = f(t_1) - Kf(t_1) = f(t_1)(1 - K) \quad (\text{B9})$$

Dividing by $(1 - K)$ gives

$$f(t_1) = \frac{f(t_1) - f(t_2)}{1 - K} \quad (\text{B10})$$

Equation (B10) expresses $f(t_1)$ as the difference of the function at two known times, t_1 and t_2 . This result was used to calculate successive points of the exponential. The exponential was then subtracted from the flight record to obtain the corrected crossing.

The time constant of the detector and the location of the upper half-power frequency point of the amplifier cause the output to be delayed in time with respect to the input, as well as distorted at the beginning and at the end of the ramp (ref. 9). The delay can be determined from the detector time constant and the amplifier upper half-power frequency point. For an n-pole system, the delay is given as

$$\Delta t = \frac{n}{2\pi f_c} \quad (\text{B11})$$

where the corner frequency f_c is the half-power frequency point of each pole. Hence, for the 3-pole system employed in the X-15 radiometer

$$t_{\text{delay}} = \text{Detector time constant} + \frac{3}{2\pi f_c} \quad (\text{B12})$$

or

$$t_{\text{delay}} = 4.94 \text{ msec} \quad (\text{B13})$$

Once the amount of delay is known it can be subtracted during data reduction so that the correct relation is reestablished between the radiometer line of sight and the radiance measurements. This correction enables the altitude of the horizon profile to be fixed with respect to earth. As indicated previously the characteristics for the far infrared flights are similar to those of the near infrared mission. Parameters for the far infrared flights are shown in table I. The sensitivity of the thermistor bolometer is two orders of magnitude below that of lead sulfide, and because of the higher low-frequency noise the low-frequency cutoff of the amplifier was increased by a factor of 20.

Calibration

The exact voltage output of the radiometers as a function of radiant power incident on the entrance aperture must be determined. The responsivity of the radiometer is affected by such factors as mirror reflectivity, stray radiation, minute misalignment of

APPENDIX B

the optical elements, and other parameters which are difficult to control and calculate. Therefore, the radiometers must be calibrated when assembled as a unit. Three basic methods using blackbody sources of known spectral radiance $R_{\omega\lambda}$ were used to calibrate the radiometers. These blackbody reference sources have cavity temperatures controllable and known to $\pm 1^\circ\text{C}$ or better, and have emissivities of 0.98 or greater. Each of the three methods was used to calibrate the radiometers, and by cross-checking the data obtained from each method confidence is gained in the accuracy of the results. Before each method can be discussed, a general equation for radiative power transfer between two surfaces must be derived.

The spectral radiant power emitted from an elemental area $dA_{(\text{surface } 1)}$ at temperature $T_{(\text{surface } 1)}$ having a spectral radiance $R_{\omega\lambda(\text{surface } 1)}$ into a solid angle $d\omega$ is (ref. 7)

$$d^4P_{\lambda(\text{surface } 1)} = R_{\omega\lambda(\text{surface } 1)} dA_{(\text{surface } 1)} d\omega \quad (\text{B14})$$

The notation $d^4P_{\lambda(\text{surface } 1)}$ indicates four integrations, two over the area $A_{(\text{surface } 1)}$ and two over the solid angle ω . The term $R_{\omega\lambda(\text{surface } 1)}$ is the spectral radiance of surface 1, which can be a blackbody source. If the temperature and emissivity of the blackbody source are known, the spectral radiance is obtainable from either normalized blackbody tables or a radiation slide rule. The spectral radiant power emitted by $dA_{(\text{surface } 1)}$ that is intercepted by a second surface is

$$d^4P_{\lambda(\text{surface } 1 \text{ to } 2)} = R_{\omega\lambda(\text{surface } 1)} dA_{(\text{surface } 1)} d\omega_{(\text{surface } 2)} \quad (\text{B15})$$

where $d\omega_{(\text{surface } 2)}$ is the solid angle subtended by the receiving second surface at $dA_{(\text{surface } 1)}$. If optical filters, such as those in the radiometers, are interposed between source and receiver, their spectral transmission η must be included and equation (B15) becomes

$$d^4P_{\lambda(\text{surface } 1 \text{ to } 2)} = \eta R_{\omega\lambda(\text{surface } 1)} dA_{(\text{surface } 1)} d\omega_{(\text{surface } 2)} \quad (\text{B16})$$

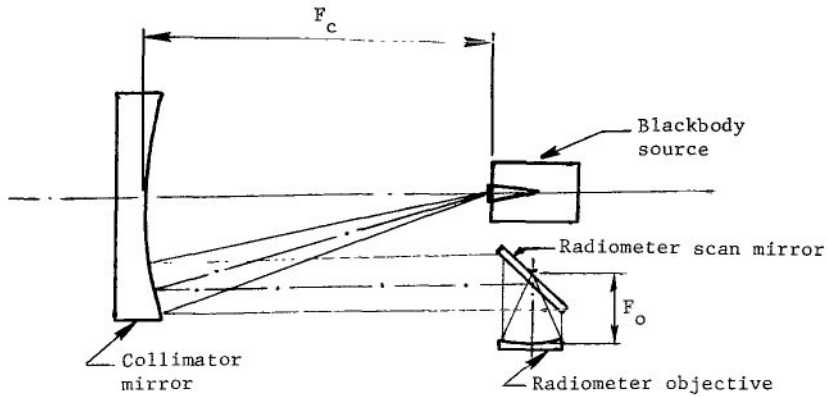
This equation may also be written as

$$d^4P_{\lambda(\text{receiver})} = \eta R_{\omega\lambda(\text{source})} dA_{(\text{source})} d\omega_{(\text{receiver})} \quad (\text{B17})$$

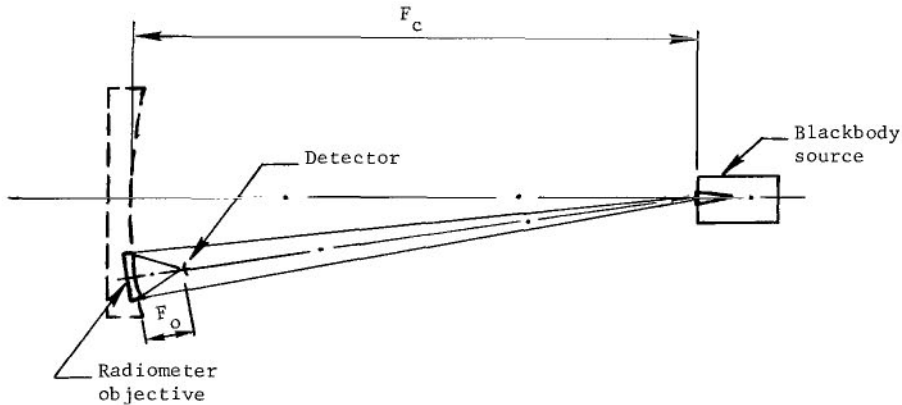
Equation (B17) will now be used to discuss the three calibration methods.

Collimated-beam method.- Figure 19(a) shows the experimental setup for the collimated-beam method of calibration. The radiation is parallel (collimated) for the

APPENDIX B



(a) Experimental setup.



(b) Simplified schematic of radiation transfer.

Figure 19.- Collimated-beam method of calibration.

path between the collimator mirror and the radiometer objective. Therefore, from the standpoint of radiation transfer, the configuration may be changed to that of figure 19(b) for which equation (B17) is true. The area of the source in equation (B17) is the effective area of the blackbody source, which includes all points of the source from which radiation reaches the detector. By using simple ray tracing the effective area of the blackbody source is seen to be the area of the detector multiplied by the magnification of the optics. Then by assuming that this image of the detector is smaller than the source, the following relation is true:

$$dA_{(\text{source})} = dA_{(\text{detector})} \frac{F_c^2}{F_o^2} \quad (\text{B18})$$

APPENDIX B

Also, $d\omega_{(\text{receiver})}$ is the solid angle subtended by the radiometer objective at the source expressed as

$$d\omega_{(\text{receiver})} = \frac{dA_{(\text{objective})}}{F_c^2} \quad (\text{B19})$$

Now,

$$d^4P_{\lambda(\text{detector})} = \eta R_{\omega\lambda(\text{source})} dA_{(\text{detector})} \frac{F_c^2}{F_o^2} \frac{dA_{(\text{objective})}}{F_c^2} \quad (\text{B20})$$

which can be simplified to

$$d^4P_{\lambda(\text{detector})} = \frac{\eta R_{\omega\lambda(\text{source})} dA_{(\text{detector})} dA_{(\text{objective})}}{F_o^2} \quad (\text{B21})$$

By definition, the solid angle $d\omega_v$ of the radiometer is $\frac{dA_{(\text{detector})}}{F_o^2}$, and therefore

$$d^4P_{\lambda(\text{detector})} = \eta R_{\omega\lambda(\text{source})} dA_{(\text{objective})} d\omega_v \quad (\text{B22})$$

The spectral radiant power on the detector is then expressed as

$$P_{\lambda(\text{detector})} = \eta R_{\omega\lambda(\text{source})} \iint_{\text{surface}} dA_{(\text{objective})} \iint_{\text{solid angle}} d\omega_v \quad (\text{B23})$$

or

$$P_{\lambda(\text{detector})} = \eta R_{\omega\lambda(\text{source})} A_{(\text{objective})} \omega_v \quad (\text{B24})$$

The electrical output of the radiometer is measured as a function of radiant power on the detector calculated by using equation (B24). This measurement may be repeated for several temperatures of blackbody sources so that the radiometer responsivity as a function of energy level is determined.

Extended-area blackbody-source method.- The extended-area blackbody-source method requires a source larger than the objective of the radiometer. The radiometer is focused at infinity; therefore, the objective projects each elemental area of the detector in a parallel, unchanging beam between objective and source. The dimension l in figure 20 can, therefore, be made zero without changing the problem. Then in equation (B17), $dA_{(\text{source})}$ is equal to $dA_{(\text{objective})}$. Also, the size of the receiver as seen from the source $d\omega_{(\text{receiver})}$ is $\frac{dA_{(\text{detector})}}{F_o^2}$. Equations (B21) and (B24) are repeated here for convenience:



APPENDIX B

$$d^4P_{\lambda(\text{detector})} = \frac{\eta R_{\omega\lambda(\text{source})} dA_{(\text{detector})} dA_{(\text{objective})}}{F_o^2}$$

and

$$P_{\lambda(\text{detector})} = \eta R_{\omega\lambda(\text{source})} A_{(\text{objective})} \omega_v$$

As discussed for the collimated-beam method, radiometer responsivity as a function of irradiance can be found by using equation (B24). This method of calibration is simple to implement in the laboratory because the radiant power on the detector is independent of l . A problem with this method is that it is very difficult to obtain an extended-area blackbody source with constant temperature and emissivity over its entire radiating surface.

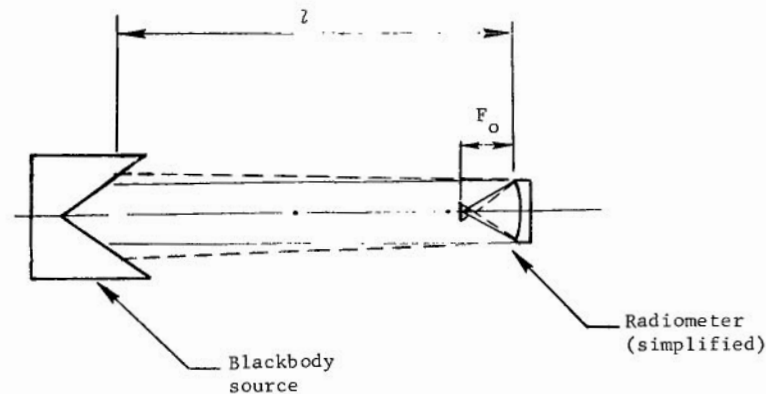


Figure 20.- Extended-area blackbody-source method of calibration.

The Jones method.- The Jones method may be considered to be a special case of the extended-area blackbody-source method. As before, optical ray tracing can be used to show that in calculating radiant energy transfer, dimension l in figure 21 may be set

equal to zero. Also $d\omega_{(\text{receiver})} = \frac{dA_{(\text{detector})}}{F_o^2}$, and equation (B17) yields

$$d^4P_{\lambda(\text{detector})} = \frac{\eta R_{\omega\lambda(\text{source})} dA_{(\text{source})} dA_{(\text{detector})}}{F_o^2} \quad (\text{B25})$$

where $\frac{dA_{(\text{detector})}}{F_o^2} = d\omega_v$. Therefore,

$$d^4P_{\lambda(\text{detector})} = \eta R_{\omega\lambda(\text{source})} d\omega_v dA_{(\text{source})} \quad (\text{B26})$$

and

$$P_{\lambda(\text{detector})} = \eta R_{\omega\lambda(\text{source})} \omega_v A_{(\text{source})} \quad (\text{B27})$$

APPENDIX B

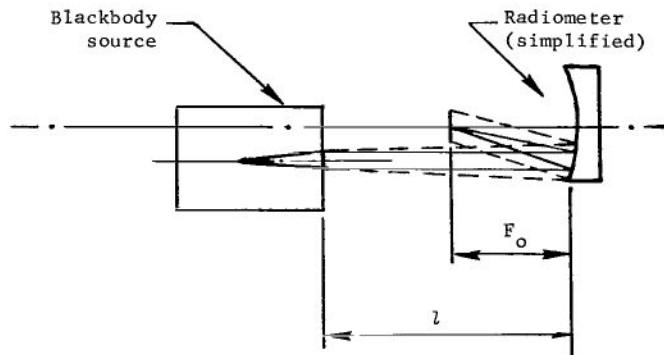


Figure 21.- Jones method of calibration.

The advantage of this method is that use can be made of a small-diameter blackbody source which is more readily available than extended-area sources. As a result of the geometry, only a small portion of the collecting area of the optics is used, and, thus, the spectral radiant emittance R_λ of the blackbody must be higher than in the previous methods to obtain the same irradiance on the detector. Because of the high-energy density of the beam the effects of stray radiation may be appreciable and thus reduce the accuracy of the method. The results of the calibration of the radiometers are shown in figure 22. The data from the 10 to 14 μm and 14 to 20 μm spectral intervals were supplied to Langley Research Center by Lockheed Missiles & Space Company under NASA Contract NAS1-4932. The power on the detector, in watts, can be obtained from the effective radiance used in figures 7, 9, and 11 by multiplying the effective radiance by the aperture area and the field of view of the radiometer. The results of the collimated-beam method and the extended-area blackbody-source method are seen to agree quite well for the three spectral intervals. The results of the Jones method are shown to be in disagreement, which can be explained by the difficulties with this method previously mentioned. For interpretation of the flight measurements, calibration results from only the collimated-beam and extended-area blackbody-source methods were used.

APPENDIX B

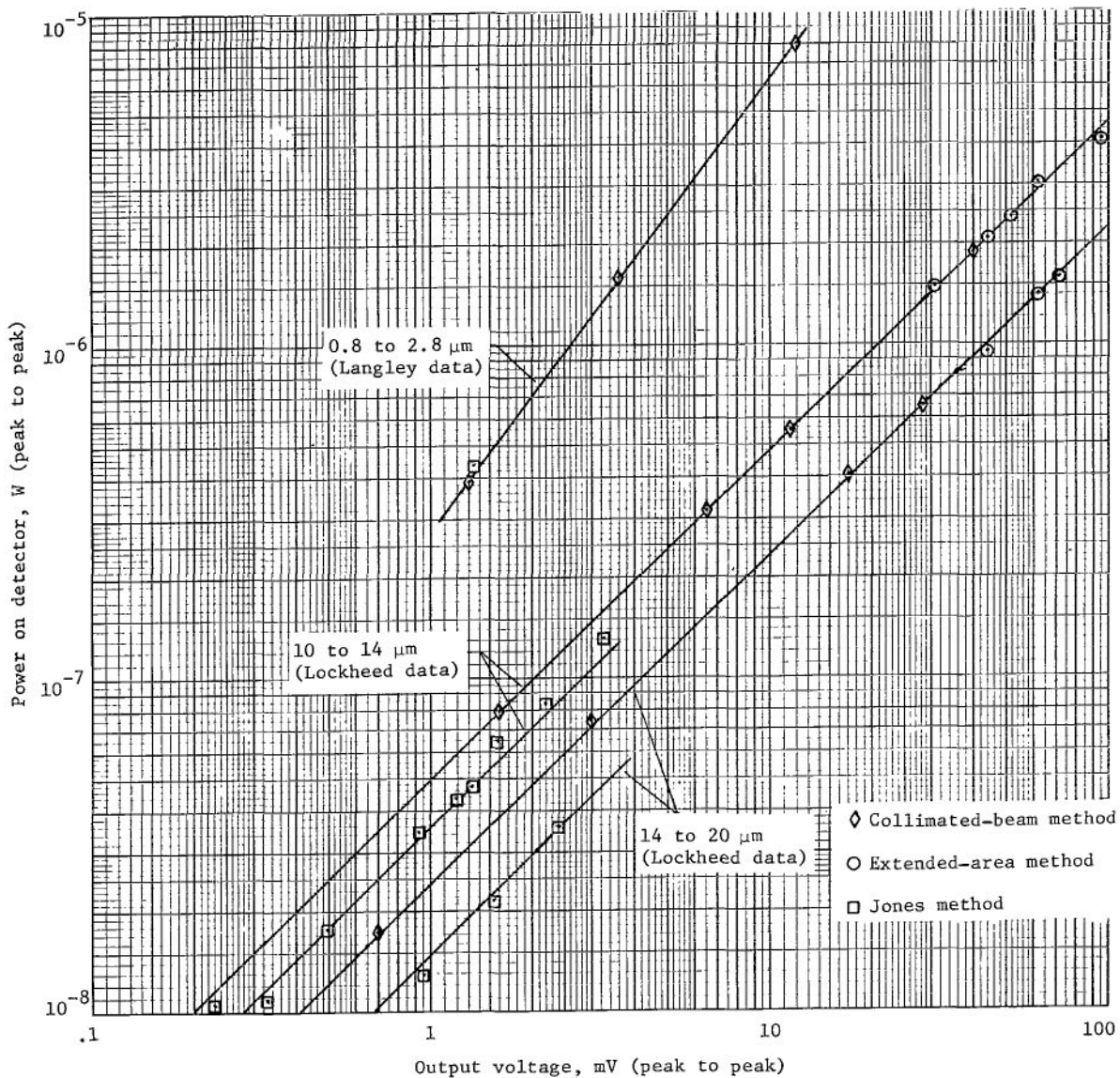


Figure 22.- Radiometer responsivity for each spectral interval.

APPENDIX C

METEOROLOGICAL DATA AND METHODS USED IN DERIVATION OF MODEL ATMOSPHERES

Meteorological data are required for the evaluation of the horizon data of the radiometer. These data include temperature and water-vapor mixing-ratio profiles from the surface to 50 km or higher and cloud-cover charts (nephanalyses) for the general area viewed by the radiometer. A discussion of the data sources, the raw data, the temperature and water-vapor vertical profiles, and essential nephanalyses are given in this appendix.

Data Sources

Temperature.- Rawinsonde data from U.S. Weather Bureau and military weather stations in the X-15 flight area are available daily for heights up to approximately 30 km. Meteorological Rocket Network (MRN) soundings are made regularly on Monday, Wednesday, and Friday at the White Sands Missile Range, New Mexico, and at Point Mugu, California. When the X-15 flight is made on other days, special rocket soundings are requested. Thus, temperature and wind measurements for heights up to 50 km or higher are made.

Mixing ratio.- The mixing ratio of CO₂ is assumed constant at 314 parts per million. The mixing ratio of water vapor may be derived from the dewpoint data gained from rawinsondes for heights up to about 10 km. Above this altitude, no humidity data is obtained on a regular basis.

Clouds.- Horizontal weather depiction charts of the U.S. Weather Bureau, and nephanalyses from ESSA's National Environmental Satellite Center served as the bases for the modified nephanalyses presented in this appendix.

Standard surface temperature.- The hourly reports from each weather station in the scan area were used to derive the standard surface temperature (4 ft above ground level).

General Meteorological Conditions

The standard meteorological charts showed that for each flight a high-pressure cell was dominating the flight area. Therefore, the area was largely free of clouds in each case. But knowledge of even scattered cloud conditions is essential, especially in the analysis of radiance data for the 0.8 to 2.8 μm and the 10 to 14 μm interval flights. Therefore, simplified nephanalyses were prepared with the aid of U.S. Weather Bureau horizontal weather depiction charts and Tiros nephanalyses for each flight day. Viewing

APPENDIX C

the motion-picture films from each mission added knowledge of small-scale cloud structure to the general picture given by the more standard weather maps. Because the radiometer in the 10 to 14 μm spectral interval "sees" to the earth's surface, a plot of surface temperature is included on the nephelanalysis for that flight (fig. 10). The results of the cloud data for the flights are shown in figures 8, 10, and 12.

Determination of Temperature and Water-Vapor Profiles

Figure 23 shows the surface trace of the nominal flight path for the X-15 mission and describes the geographical extent of the volume of atmosphere which was sampled on a nominal X-15 sensor mission. In constructing a model that is characteristic of the atmospheric state during each flight, it is necessary to gather available data describing the state from 0 to 50 km and to interpolate these data to describe the volume being sampled. Therefore, both rawinsonde and rocketsonde data are needed because the rawinsonde data describes altitudes up to 30 km and the rocketsonde data, those above 30 km. Figure 23 shows the rawinsonde sites chosen were Salt Lake City, Utah, and Las Vegas, Nevada. The nearest rocketsonde sites are Point Mugu, California, and White Sands Missile Range, New Mexico. Because all flights occurred between 12:00 and 00:00 Greenwich Mean Time (GMT), the derivation of a model atmosphere at rawinsonde altitudes is amenable to temporal interpolations between 12:00 and 00:00 GMT and spatial interpolations between Salt Lake City and White Sands Missile Range.

The rocketsonde sites are displaced geographically farther from the scan area than is desirable. Nevertheless, a spatial interpolation and extrapolation of rocketsonde data was performed to yield an estimate of conditions over the scan area at levels higher than 30 km. Where overlap in rocketsonde and rawinsonde data occurred, the rocketsonde data were adjusted to the rawinsonde data. Where the published MRN data lacked a temperature correction, the Wagner temperature-correction criterion was applied (refs. 10 and 11).

The basic data from both rawinsondes and rocketsondes are plotted in figures 24, 25, and 26 for flights 1, 2, and 3, respectively. In flight 1, data from only one rocketsonde are available. In this flight, of course, no interpolation of rocket data was possible and, therefore, the model data derived are less accurate.

In figures 24, 25, and 26, pressure is plotted against measured temperature. Both rawinsonde and rocketsonde data for each flight are plotted on the same chart. It should be noted, however, that for the rawinsonde data, pressure is a directly measured quantity, whereas for the rocketsonde, it is a derived quantity. The accuracy of all temperature data plotted is estimated to be as follows:

For rawinsonde data

$\pm 1^{\circ}$ K up to 12 mbar (nominal 30 km)

APPENDIX C

and for rocketsonde data

$\pm 2^{\circ}$ K at 12 mbar (nominal 30 km)

$\pm 3^{\circ}$ K at 3 mbar (nominal 40 km)

$\pm 6^{\circ}$ K at 0.8 mbar (nominal 50 km)

$\pm 9^{\circ}$ K at 0.2 mbar (nominal 60 km)

For similar studies, see references 10 and 11.

Calculation of the Water-Vapor Mixing Ratio

Because the meteorological rockets carried no moisture-sensing instruments, the sole water-vapor data available were obtained from the Las Vegas and Salt Lake City rawinsonde data. These gave dewpoint information up to approximately 300-mbar altitude (nominal 10 km). Above this altitude, the nature of the water-vapor content of the stratosphere is unknown, and existing observations have given rise to contradictory interpretations (ref. 12). Therefore the values derived here must be regarded only as estimates based on one of the existing models. The water-vapor mixing ratios against altitude were derived by the following procedure:

(1) Plots of dewpoint against altitude were made for 00:00 and 12:00 GMT for both stations, and a mean curve was then selected.

(2) The saturation vapor pressure corresponding to this dewpoint is read from the Smithsonian Meteorological Tables (ref. 13). Saturation vapor pressure over water was used for temperatures $\geq -40^{\circ}$ C, the saturation vapor pressure over ice was used for temperatures $< -40^{\circ}$ C.

(3) The mixing ratio w is given by $w = 621 \frac{e}{p - e}$, where e is the water-vapor pressure at the dewpoint temperature at the given altitude. The units are grams of water vapor per kilogram of air.

(4) Above the peak altitude of moisture data in each case, assumed curves were used. These curves were derived in different ways. In the 0.8 to 2.8 μm and 10 to 14 μm flights, insufficient moisture data were obtained for any extrapolation. Therefore, in these cases the midlatitude mixing-ratio model of the Handbook of Geophysics was used (ref. 14). For the 14 to 20 μm spectral interval the mixing ratio profile was obtained by extrapolating above the last data point. This profile is parallel to the previously mentioned midlatitude model. In every case, above 10 mbar (nominal 31 km) the mixing ratio is assumed constant to the top of the model atmosphere.

The resulting mixing ratios are given in the final model atmospheres for flights 1, 2, and 3 in tables II, III, and IV, respectively.

APPENDIX C

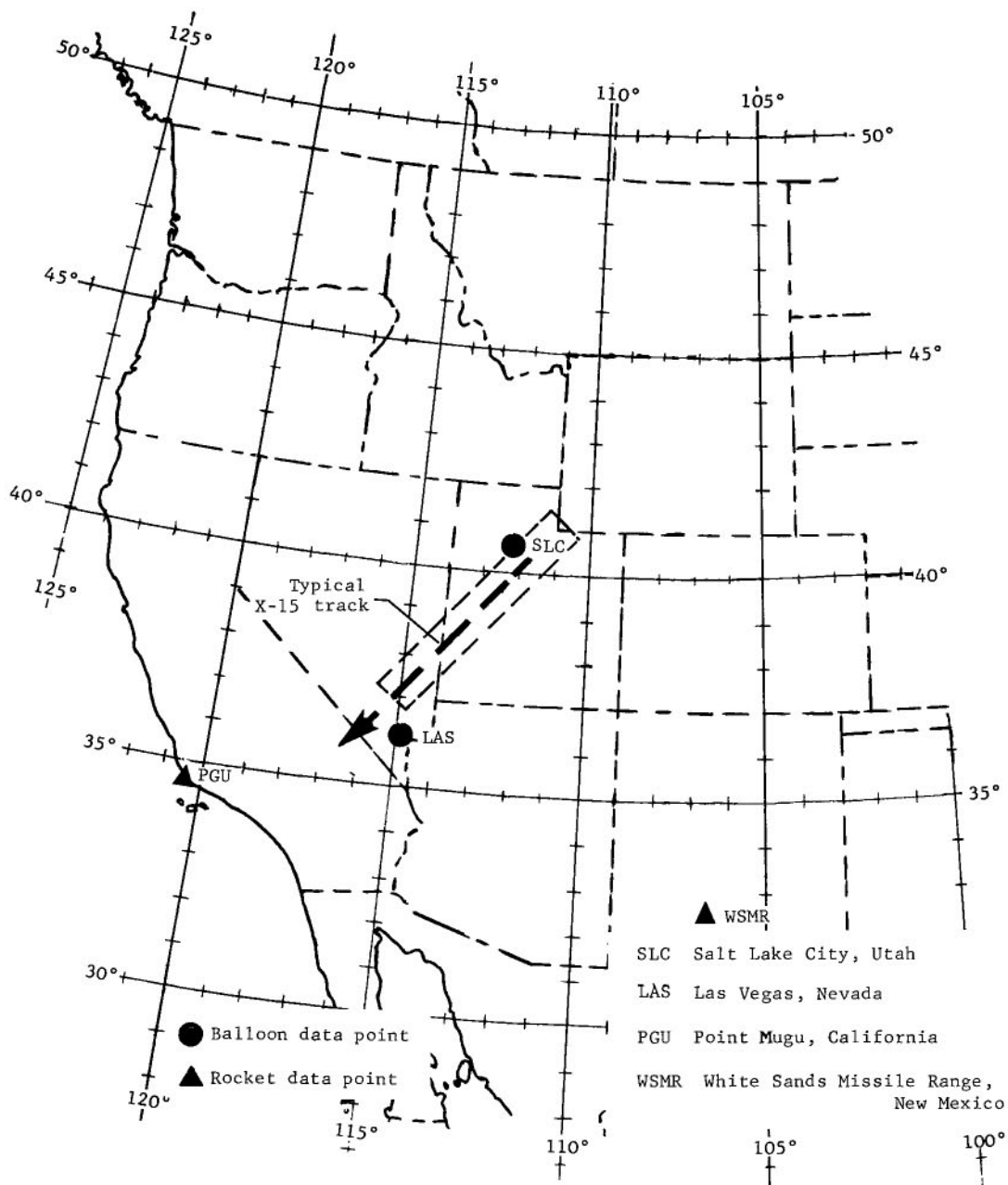


Figure 23.- Typical flight path of X-15, showing location of balloon and rocket sounding stations yielding data for model-atmosphere construction.

APPENDIX C

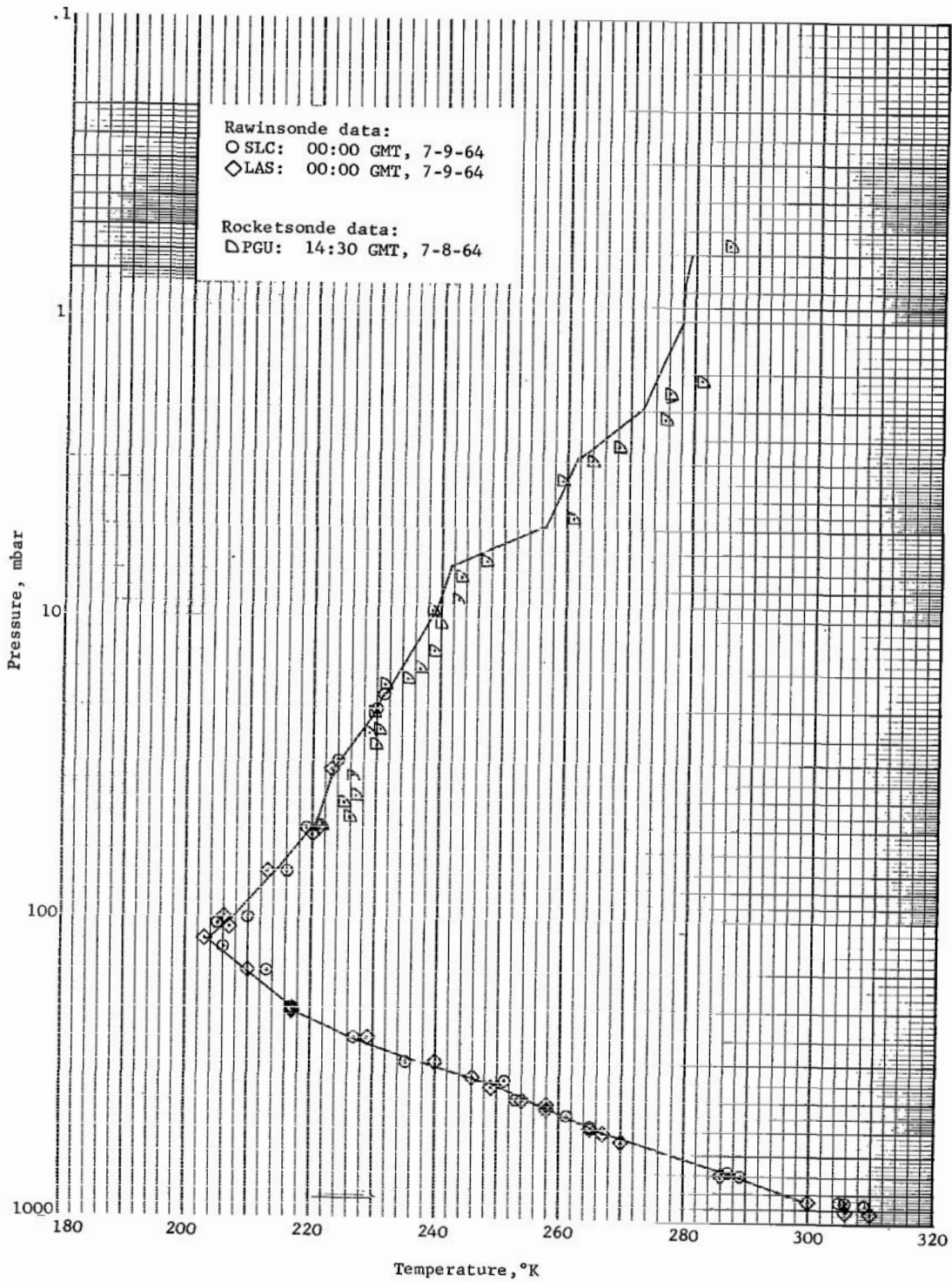


Figure 24.- Pressure-temperature data used in derivation of model atmosphere for 0.8 to 2.8 μm spectral interval. Flight 1; July 8, 1964.

APPENDIX C

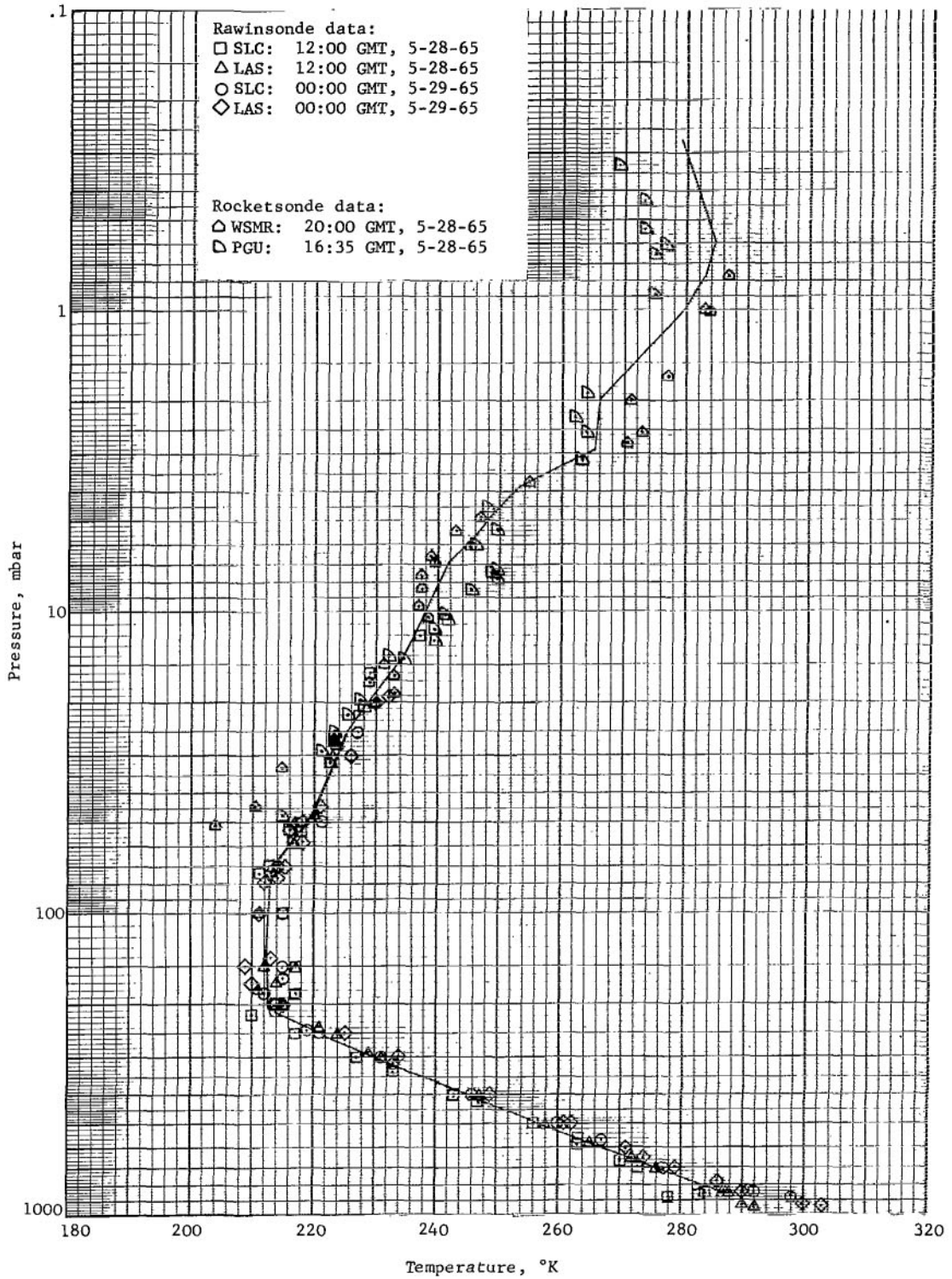


Figure 25.- Pressure-temperature data used in derivation of model atmosphere for 10 to 14 μ m spectral interval. Flight 2; May 28, 1965.

APPENDIX C

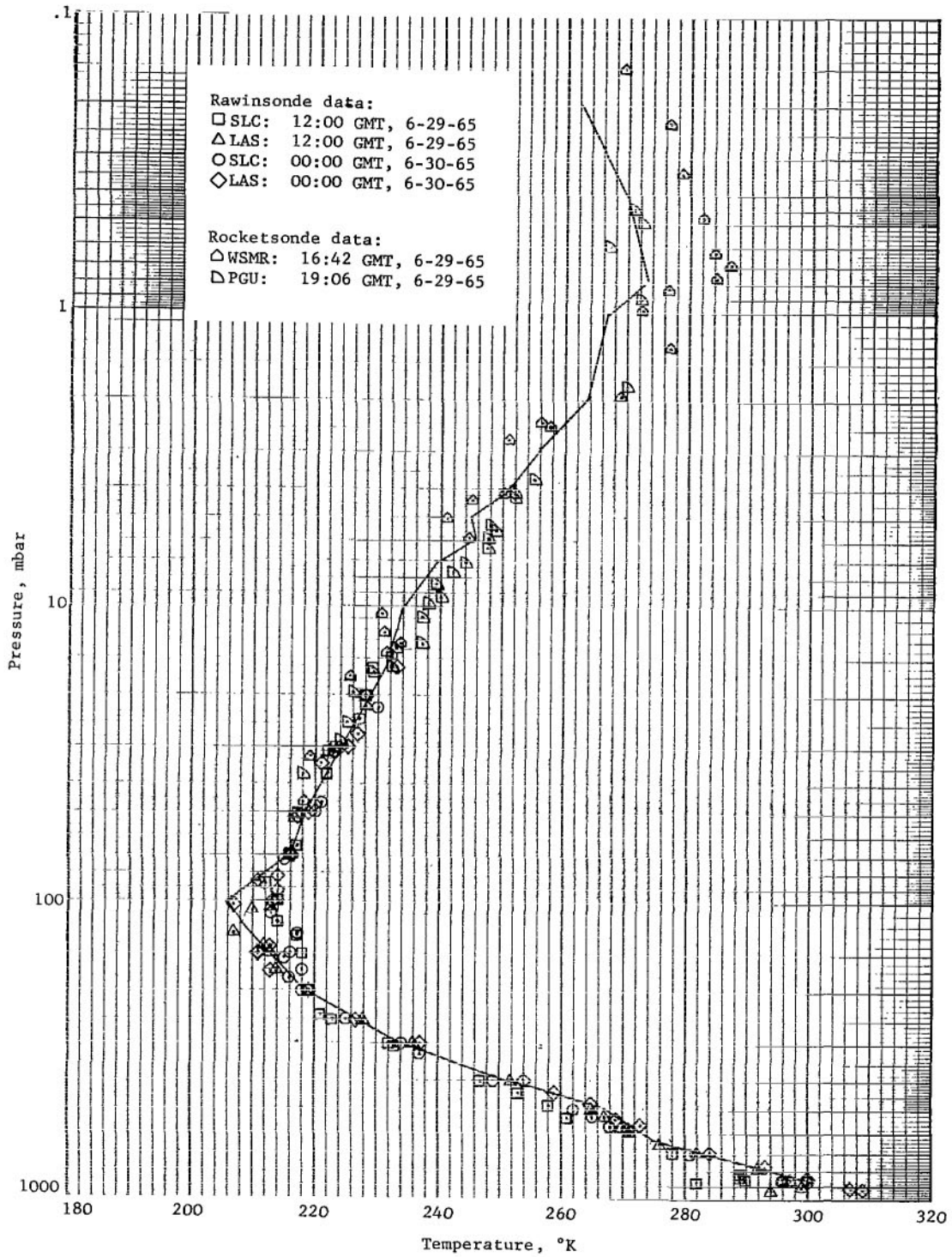


Figure 26.- Pressure-temperature data used in derivation of model atmosphere for 14 to 20 μm spectral interval. Flight 3; June 29, 1965.

APPENDIX D

ACCURACY ANALYSIS OF THE EXPERIMENTAL SYSTEM

The measured radiance profiles are subject to errors introduced by the accuracy of the equipment and to errors that arise in reading the flight records. Random errors in tangent height are caused by fluctuations in the X-15 pitch-angle and roll-angle data, the radiometer scan-mirror-position data, and the accuracy of X-15 altitude radar data. Precise knowledge of tangent height is also affected by bias errors such as the mounting angle of the radiometer on the X-15 and stable platform mounting and calibration accuracy. The effect of random error due to fluctuations can be estimated by using statistical methods; the bias error, estimated from experience.

To determine the standard deviation of the X-15 attitude data for the present experiment, a smooth least-squares error curve is fitted to the pitch-angle and roll-angle data. Then δX_N , the difference between the fitted curve and the actual curve at each point N from this the standard deviation σ can be found by using the following equation:

$$\sigma = \sqrt{\frac{\sum_{N=1}^N (\delta X_N)^2}{N-1}}$$

where N is the number of samples (ref. 15). By using this procedure and the flight record, the standard deviations of the pitch and roll angles were found to be

$$\sigma_{\theta} = 0.111^{\circ}$$

$$\sigma_{\phi} = 0.111^{\circ}$$

The random error of the scan-mirror angle was determined in the same manner, and resulted in $\sigma_{\alpha} = 0.097^{\circ}$. From experience and from discussion with the X-15 range operator, the radar-measurement accuracy is estimated to have a value of

$$\sigma_{h_{X-15}} = 0.12 \text{ km.}$$

The bias errors cannot be measured but must be estimated. The stable-platform bias including installation alignment and recording film shrinkage was estimated to be $\sigma_{\theta_C} = 0.08^{\circ}$. The angle between the X-15 center line and the radiometer is determined by using a theodolite. The $1 - \sigma$ accuracy of this measurement is estimated to be 0.033° . To find how these errors affect the tangent height h use is made of the error-propagation equation

$$\sigma_h = \sqrt{\left(\frac{\partial h}{\partial \theta}\right)^2 \sigma_{\theta}^2 + \left(\frac{\partial h}{\partial \phi}\right)^2 \sigma_{\phi}^2 + \left(\frac{\partial h}{\partial \alpha}\right)^2 \sigma_{\alpha}^2 + \left(\frac{\partial h}{\partial h_{X-15}}\right)^2 \sigma_{h_{X-15}}^2 + \left(\frac{\partial h}{\partial \alpha_m}\right)^2 \sigma_{\alpha_m}^2 + \left(\frac{\partial h}{\partial \theta_C}\right)^2 (\sigma_{\theta_C})^2} \quad (D1)$$

APPENDIX D

which applies to linear error analysis when independence is assumed. The term $\frac{\partial h}{\partial \theta}$ is obtained from the equation for h and evaluated at a point where the nominal value of each parameter is known. The value of h is given by equation (A17) as

$$h = \left[\sin \left(\cos^{-1} \left\{ \sin \theta \cos \psi_m \cos(\alpha + \alpha_m) + \cos \theta \left[\sin \phi \sin \psi_m \cos(\alpha + \alpha_m) + \cos \phi \sin(\alpha + \alpha_m) \right] \right\} \right) \right] (h_{X-15} + r) - r$$

Taking the partial derivative gives

$$\frac{\partial h}{\partial \theta} = \frac{-(K_1 \sin \theta + K_2 \cos \theta)(K_1 \cos \theta - K_2 \sin \theta)(h_{X-15} + r)}{\sqrt{1 - (K_1 \sin \theta + K_2 \cos \theta)^2}} \quad (D2)$$

where

$$K_1 = \cos \psi_m \cos(\alpha + \alpha_m) \quad (D3)$$

and

$$K_2 = \sin \phi \sin \psi_m \cos(\alpha + \alpha_m) + \cos \phi \sin(\alpha + \alpha_m) \quad (D4)$$

By using the following nominal values:

$$\theta = -4.1^\circ$$

$$\psi_m = 1^\circ 26'$$

$$\alpha = 12^\circ$$

$$\alpha_m = -2^\circ 17'$$

$$\phi = -0.2^\circ$$

$$h_{X-15} = 70 \text{ km}$$

$$r = 6371 \text{ km}$$

The sensitivity coefficient becomes $\frac{\partial h}{\partial \theta} = 10.98 \text{ km/deg}$. The other sensitivity coefficients in equation (D1) may be found similarly. For the above parameters they are

$$\frac{\partial h}{\partial \phi} = 0.34 \text{ km/deg}$$

$$\frac{\partial h}{\partial \alpha} = 10.87 \text{ km/deg}$$

APPENDIX D

$$\frac{\partial h}{\partial h_{X-15}} = 0.98 \text{ km/km}$$

$$\frac{\partial h}{\partial \alpha_m} = 10.87 \text{ km/deg}$$

$$\frac{\partial h}{\partial \theta_C} = 10.98 \text{ km/deg}$$

By using the errors and sensitivity coefficients, the total estimated standard deviation σ_h is then found to be 1.87 km. If the distribution is assumed to be normal, then 95.4 percent of the measured points will be within 2σ of the mean. If this is taken as the criterion, the accuracy of the data is ± 3.74 km. The estimated accuracy will change as the flight conditions change. However, for the X-15 the desirable data are gathered during the 30-sec range about peak altitude so that changes in the flight conditions are small. Thus, ± 3.74 km is a good estimate of the experimental accuracy for all the radiance profiles obtained.

An estimate of the accuracy of the radiometric calibration may be obtained from the data shown in figure 22. The standard deviation σ of the individual calibration points may be determined in a manner similar to that performed for the aircraft-attitude data. For the extended-area and collimated-beam methods and the 14 to 20 μm interval radiometer, $2\sigma = 0.0376 \mu\text{W}$. Full-scale signal during flight is approximately $0.3 \mu\text{W}$, so that the percent error is $\frac{0.0376}{0.3} \times 100 = 12.5$. The accuracy of the flight tape recorder and data-reduction digitizer is thought to be 2 percent, and, thus, the overall radiometric accuracy becomes 14.5 percent.

REFERENCES

1. Mellinger, G. R.: Design and Operation of the X-15 Hypersonic Research Airplane. AGARD Rep. 288, Oct. 1960.
2. Hanel, R. A.; Bandeen, W. R.; and Conrath, B. J.: The Infrared Horizon of the Planet Earth. NASA TN D-1850, 1963.
3. Wark, D. Q.; Alishouse, J.; and Yamamoto, G.: Variation of the Infrared Spectral Radiance Near the Limb of the Earth. Appl. Opt., vol. 3, no. 2, Feb. 1964.
4. Kondratiev, K. Y.; and Yakushevskaya, K. E.: Angular Distribution of the Outgoing Thermal Radiation in the Different Regions of the Spectrum. First International Symposium on Rocket and Satellite Meteorology, H. Wexler and J. E. Caskey, Jr., eds., John Wiley & Sons, Inc., 1963, pp. 254-277.
5. McKee, Thomas B.; Whitman, Ruth I.; and Engle, Charles D.: Radiometric Observations of the Earth's Horizon From Altitudes Between 300 and 600 Kilometers. NASA TN D-2528, 1964.
6. Feoktistov, K. P.; Rozenberg, G. V.; Sandomirsky, A. B.; Sergeyeovich, V. N.; and Sonechkin, D. M.: Some of the Results of Observations Conducted During the Flight of the Spaceship "Voskhod." Problems of Atmospheric Circulation, R. V. Garcia and T. F. Malone, eds., Spartan Books, 1966, pp. 176-186.
7. Kruse, Paul W.; McGlauchlin, Laurence D.; and McQuistan, Richmond B.: Elements of Infrared Technology. John Wiley & Sons, Inc., 1963.
8. Schwartz, Mischa: Information Transmission, Modulation and Noise. McGraw-Hill Book Co., Inc., 1959.
9. Millman, Jacob; and Taub, Herbert: Pulse and Digital Circuits. McGraw-Hill Book Co., Inc., 1956.
10. Clark, George Q.; and McCoy, John G.: Measurement of Stratospheric Temperature. J. Appl. Meteorol., vol. 4, no. 3, June 1965, pp. 365-370.
11. Wagner, N. K.: Theoretical Accuracy of a Meteorological Rocketsonde Thermistor. J. Appl. Meteorol., vol. 3, no. 4, Aug. 1964, pp. 461-469.
12. Craig, Richard A.: The Upper Atmosphere - Meteorology and Physics. Academic Press, Inc., c.1965.
13. List, Robert J.: Smithsonian Meteorological Tables. Sixth revised ed., Smithsonian Inst., 1951.

14. Anon.: Handbook of Geophysics. Revised ed., Macmillan Co., 1960.
15. Beers, Yardley: Introduction to the Theory of Error. Addison-Wesley Pub. Co., Inc., c.1957.

TABLE I.- RADIOMETER CHARACTERISTICS

	Flight 1 - July 8, 1964	Flight 2 - May 28, 1965	Flight 3 - June 29, 1965
Spectral region	0.8 to 2.8 μm	10 to 14 μm	14 to 20 μm
Aperture	12.7-cm diameter	12.7-cm diameter	12.7-cm diameter
Focal length	12.7 cm	12.7 cm	12.7 cm
Field of view	0.13 $^\circ$ by 0.13 $^\circ$	0.13 $^\circ$ by 0.13 $^\circ$	0.13 $^\circ$ by 0.13 $^\circ$
Scan angle	30 $^\circ$	30 $^\circ$	30 $^\circ$
Scan speed	20 $^\circ$ /sec	20 $^\circ$ /sec	20 $^\circ$ /sec
Filter	Color filter (3 mm)	Interference and absorption (1 mm)	Interference and absorption (1 mm)
Radiometer relative spectral response	Figure 6(a)	Figure 6(b)	Figure 6(c)
Peak transmission of optics	0.87	0.62	0.29
Detector	Lead sulfide (0.3 mm by 0.3 mm)	Thermistor bolometer (0.3 mm by 0.3 mm)	Thermistor bolometer (0.3 mm by 0.3 mm)
Noise equivalent power	2.4×10^{-10} W/Hz $^{1/2}$	3.4×10^{-8} W/Hz $^{1/2}$	2.5×10^{-8} W/Hz $^{1/2}$
Detectivity	1.45×10^9 cm-Hz $^{1/2}$ /W	1.01×10^7 cm-Hz $^{1/2}$ /W	1.39×10^7 cm-Hz $^{1/2}$ /W
Electronics bandpass	0.01 to 220 Hz	0.2 to 220 Hz	0.2 to 220 Hz
Detector time constant	2.75 msec	2.8 msec	2.4 msec

TABLE II.- MODEL ATMOSPHERE FOR 0.8 TO 2.8 μm SPECTRAL INTERVAL
 [00:00 GMT, July 9, 1964]

Pressure, mbar	Temperature, $^{\circ}\text{K}$	Mixing ratio, w, g/kg
850	300	5.9
700	287	4.2
500	265	2.6
400	255	.8
350	248	.7
300	237	.05
250	227	.016
200	218	.016
150	210	.013
^a 118	204	.010
100	208	.0098
70	215	.014
55	219	.018
50	220	.020
30	224	.045
20	230	.068
18	231	.090
10	238	.150
7	241	
5	257	
3	261	
2	272	
1	278	
.8	278	
.6	279	

^aTropopause.

TABLE III.- MODEL ATMOSPHERE FOR 10 TO 14 μm SPECTRAL INTERVAL
 [18:00 GMT, May 28, 1965]

Pressure, mbar	Temperature, $^{\circ}\text{K}$	Mixing ratio, w, g/kg
850	289	3.20
700	276	2.53
500	258	.426
450	253	.287
400	246	.184
350	239	.062
300	231	.028
250	223	.019
^a 200	213	.0123
150	213	.0093
100	213	.0090
70	213	.0136
50	219	.0200
30	224	.037
25	225	.067
20	229	.087
15	234	.100
10	238	.150
7	242	
6	245	
5	248	
4	253	
3	265	
2	266	
1	280	
.8	283	
.6	285	
.3	280	

^aTropopause.

TABLE IV.- MODEL ATMOSPHERE FOR 14 TO 20 μm SPECTRAL INTERVAL

[18:00 GMT, June 29, 1965]

Pressure, mbar	Temperature, $^{\circ}\text{K}$	Mixing ratio, w, g/kg
850	299	4.8
700	284	3.35
650	275	2.5
500	267	.70
420	255	.45
400	251	.41
300	235	.05
200	219	.016
121	209	.010
^a 100	206	.0098
70	216	.014
50	218	.020
30	224	.045
20	229	.068
15	232	.100
10	234	.150
7	240	
6	246	
5	245	
4	252	
3	256	
2	264	
1	267	
.8	273	
.6	272	
.4	270	
.2	262	

^aTropopause.

TABLE V.- TYPICAL MEASURED PROFILES IN 0.8 TO 2.8 μm SPECTRAL INTERVAL

[Flight 1; 20:05 GMT July 8, 1964; observer altitude, 50 km]

Tangent height, km	Effective radiance, $\text{W}/\text{m}^2\text{-sr}$, for test -				
	1	2	3	4	5
2	29.4	23.6	25.1	----	----
6	31.6	30.0	22.0	24.4	40.6
10	30.5	19.3	28.2	25.6	44.7
12	15.9	12.1	24.0	29.5	53.7
14	15.2	11.6	12.5	22.2	31.5
16	11.5	8.6	11.2	9.6	16.8
18	6.2	7.6	7.2	7.9	15.0
20	3.8	5.6	4.4	4.4	12.4
25	2.7	2.5	2.4	2.0	2.6
30	2.0	2.1	2.8	.2	2.1
35	1.3	1.5	2.1	.4	1.2
40	.8	.3	1.3	.4	1.0

TABLE VI.- TYPICAL MEASURED PROFILES IN 10 TO 14 μm SPECTRAL INTERVAL
 [Flight 2; 16.47 GMT, May 28, 1965; observer altitude, 62 km]

Tangent height, km	Effective radiance, $\text{W}/\text{m}^2\text{-sr}$, for test -				
	1	2	3	4	5
-50	18.2	17.5	16.6	16.33	17.2
-45	17.9	17.35	16.5	16.33	17.1
-40	17.5	17.10	16.1	16.33	16.92
-35	17.1	16.8	15.62	16.33	16.65
-30	16.55	16.35	15.1	16.33	16.25
-25	15.95	15.87	14.55	16.33	15.83
-20	15.3	15.3	14.02	16.2	15.45
-15	14.55	14.6	13.31	15.6	14.9
-10	13.8	13.8	12.4	14.9	14.38
-5	12.8	12.6	11.6	13.8	13.5
0	11.4	10.2	10.8	12.3	12.5
5	8.25	5.15	7.6	9.7	11.07
10	3.0	2.5	3.2	4.3	8.6
15	1.6	1.8	2.4	3.0	4.7
20	1.33	1.5	2.0	2.6	3.7
25	1.12	1.3	1.7	2.3	3.02
30	.98	1.1	1.4	1.9	2.5
35	.8	.9	1.1	1.6	2.0
40	.68	.7	.85	1.3	1.6
45	.5	.5	.6	.98	1.1
50	.35	.35	.4	.68	.6
55	.18	.18	.18	.31	.25
60	0	0	0	0	0

TABLE VII.- TYPICAL MEASURED PROFILES IN 14 TO 20 μm SPECTRAL INTERVAL

[Flight 3; 17:23 GMT, June 29, 1965; observer altitude, 76 km]

Tangent height, km	Effective radiance, $\text{W}/\text{m}^2\text{-sr}$, for test -				
	1	2	3	4	5
-15	4.52	4.5	4.61	4.69	4.95
-10	4.5	4.48	4.55	4.65	4.91
-5	4.45	4.45	4.52	4.63	4.85
0	4.38	4.35	4.38	4.5	4.72
5	4.21	4.19	4.25	4.42	4.54
10	3.72	3.89	3.80	3.75	4.25
15	2.65	3.05	2.81	3.07	3.75
20	2.15	2.12	2.25	2.12	2.81
25	1.88	2.34	2.03	2.25	2.35
30	1.7	2.05	1.78	1.90	2.06
35	1.4	1.57	1.55	1.55	1.70
40	1.0	1.2	1.15	1.05	1.2
45	.55	.8	.65	.5	.75
50	.15	.25	.37	.15	.2
55	0	0	0	0	0

FIRST CLASS MAIL

070 001 45 51 3DS 68168 00903
AIR FORCE WEAPONS LABORATORY/AFWL/
KIRTLAND AIR FORCE BASE, NEW MEXICO 8711

ATTN: MISS PAULINE F. CANOVA, CHIEF TECHNICAL
LIBRARY /AFWL/

POSTMASTER: If Undeliverable (Section 15,
Postal Manual) Do Not Return

"The aeronautical and space activities of the United States shall be conducted so as to contribute . . . to the expansion of human knowledge of phenomena in the atmosphere and space. The Administration shall provide for the widest practicable and appropriate dissemination of information concerning its activities and the results thereof."

—NATIONAL AERONAUTICS AND SPACE ACT OF 1958

NASA SCIENTIFIC AND TECHNICAL PUBLICATIONS

TECHNICAL REPORTS: Scientific and technical information considered important, complete, and a lasting contribution to existing knowledge.

TECHNICAL NOTES: Information less broad in scope but nevertheless of importance as a contribution to existing knowledge.

TECHNICAL MEMORANDUMS: Information receiving limited distribution because of preliminary data, security classification, or other reasons.

CONTRACTOR REPORTS: Scientific and technical information generated under a NASA contract or grant and considered an important contribution to existing knowledge.

TECHNICAL TRANSLATIONS: Information published in a foreign language considered to merit NASA distribution in English.

SPECIAL PUBLICATIONS: Information derived from or of value to NASA activities. Publications include conference proceedings, monographs, data compilations, handbooks, sourcebooks, and special bibliographies.

TECHNOLOGY UTILIZATION PUBLICATIONS: Information on technology used by NASA that may be of particular interest in commercial and other non-aerospace applications. Publications include Tech Briefs, Technology Utilization Reports and Notes, and Technology Surveys.

Details on the availability of these publications may be obtained from:

SCIENTIFIC AND TECHNICAL INFORMATION DIVISION
NATIONAL AERONAUTICS AND SPACE ADMINISTRATION
Washington, D.C. 20546